EUROPEAN ORGANIZATION FOR NUCLEAR RESEARCH

CERN-PH-EP/2005-043
September 23, 2005

Measurement of the Mass and the Width of the W Boson at LEP

The L3 Collaboration

Abstract

The mass and the total decay width of the W boson are measured with the L3 detector at the LEP e^+e^- collider using W-boson pairs produced in 0.7 fb^{-1} of data collected at centre-of-mass energies between 161 and 209 GeV. Combining semi-leptonic and fully-hadronic final states, the mass and the width of the W boson are determined to be

$$\begin{aligned} m_{\mathrm{W}} &= 80.270 \pm 0.046 \pm 0.031 \text{ GeV} \quad \text{and} \\ \Gamma_{\mathrm{W}} &= 2.18 \pm 0.11 \pm 0.09 \text{ GeV} \quad , \end{aligned}$$

where the first uncertainty is statistical and the second systematic.

Submitted to *Eur. Phys. J. C*

1 Introduction

The mass, m_{W}, and the total decay width, Γ_{W}, are fundamental properties of the W boson. Their measurement, initially performed at the Sp$\bar{\mathrm{p}}$S hadron collider [1], provides important information about the Standard Model of electroweak interactions [2]. Together with other electroweak parameters such as the Z-boson mass, the effective weak mixing angle and the measurement of the top-quark mass [3], the precise determination of m_{W} allows a thorough test of the Standard Model at the quantum loop level as well as constraining the mass of the Higgs boson [4].

In $\mathrm{e^+e^-}$ collisions, W bosons are produced singly or in pairs. At centre-of-mass energies, $\sqrt{s}$, exceeding $2m_{\mathrm{W}}$, W-boson pair production, $\mathrm{e^+e^-} \to \mathrm{W^+W^-}$, dominates. The pair-production cross section at threshold is sensitive to m_{W}. Therefore, at LEP m_{W} was first derived from cross section measurements [5,6]. At centre-of-mass energies well above production threshold, W bosons are directly reconstructed and the effective mass of the decay products is used to determine m_{W} [7,8]. The mass distribution of the W bosons is analysed and m_{W} and Γ_{W} are determined by comparing samples of Monte Carlo events to data. A reweighting procedure is applied to obtain Monte Carlo samples corresponding to different values of m_{W} and Γ_{W}.

In the following, m_{W} and Γ_{W} are defined such that the denominator of the W-boson propagator, $(m^2 - m_{\mathrm{W}}^2) + im^2\Gamma_{\mathrm{W}}/m_{\mathrm{W}}$, models the mass-dependent width of the W boson. The analysis presented here is based on a data sample collected with the L3 detector [9] at $\sqrt{s} = 189-209$ GeV, corresponding to a total integrated luminosity of 629 pb^{-1}. These results are combined with previous L3 measurements at lower centre-of-mass energies [5,7] yielding final results on m_{W} and Γ_{W} based on the complete data sample of 706 pb^{-1} collected by the L3 experiment at $\sqrt{s} = 161-209$ GeV. Other measurements of m_{W} at LEP and the TEVATRON are described in References 8 and 10, respectively. The indirect determination of m_{W} from electroweak precision data is presented in Reference 4.

2 Data sample

W bosons decay into hadrons, mostly through $\mathrm{W^-} \to \bar{\mathrm{u}}\mathrm{d}$ or $\bar{\mathrm{c}}\mathrm{s}$, or leptons, $\mathrm{W^-} \to \ell^-\bar{\nu}_\ell$, where ℓ denotes an electron, muon or tau lepton. Charge-conjugate states are understood to be included throughout this article. In the following, these final states are denoted as qq and $\ell\nu$, or, in general, ff, for both $\mathrm{W^+}$ and $\mathrm{W^-}$ decays. W-boson pair production yields three classes of events: the fully-leptonic, $\ell\nu\ell\nu$, the semi-leptonic, $\mathrm{qq}\ell\nu$, and the fully-hadronic, qqqq, final states. Due to the presence of more than one neutrino in the $\ell\nu\ell\nu$ final state, the effective masses of the W bosons cannot be directly reconstructed from their decay products and this decay channel is not further considered here. Visible final-state fermions are reconstructed in each event. Electrons and muons from W-boson or τ-lepton decays are measured in the calorimeters and in the tracking system. Hadronically-decaying τ-leptons are identified as narrow, low-multiplicity, jets. Jets originating from quarks are reconstructed by combining information from calorimetric clusters and associated tracks into jets using the DURHAM algorithm [11].

The data analysed correspond to seven average values of $\sqrt{s}$, listed in Table 1. The selection of W-boson pair-production events is described in Reference 12. The selection of the $\mathrm{qqe}\nu$ and $\mathrm{qq}\mu\nu$ final states requires an identified high-energy electron or muon, respectively. The $\mathrm{qq}\tau\nu$ final state is characterised by a low-energy isolated electron or muon or by the reconstruction of a narrow jet. For all semi-leptonic final states, missing momentum due to the neutrino is required and the jet-jet mass has to be compatible with m_{W}. The selection of the qqqq final

state requires events with high multiplicity, small missing energy and a four-jet topology. To reject quark-pair production with additional jets originating from radiated gluons an artificial neural network is trained using discriminating variables such as the jet energies, broadenings and angles, the event spherocity, the jet multiplicity and the DURHAM jet-resolution parameter for which the event topology changes from three to four jets, y_{34}. Only events with high neural-network output are retained for further analysis. The numbers of selected W-boson pairs are detailed in Table 1.

3 Monte Carlo simulation

The KANDY [13] Monte Carlo generator is used to model four-fermion production, including both W-boson production and background processes. The RACOONWW [14] program is used as a cross check and to estimate possible systematic uncertainties due to the modelling of photon radiation. Additional background contribution from fermion-pair production, dominated by the $e^+e^- \to qq$ process, is simulated using the KK2F [15] event generator. Monte Carlo events are generated at the seven average $\sqrt{s}$ values listed in Table 1. Effects from the spread of centre-of-mass energies within the individual energy points are found to be negligible. The expected number of background events is listed in Table 1.

The hadronisation process is modelled with the PYTHIA [16] program, while the HERWIG [17] and ARIADNE [18] programs are used to assess systematic uncertainties. These Monte Carlo programs are tuned to describe hadronic Z-boson decays recorded at the Z resonance [19]. In the case of W-boson pair production, a dedicated parameter set, tuned only on Z-boson decays into light-quarks (u,d,c,s) is used.

Bose-Einstein correlations (BEC) [20] in W-boson decays are simulated using the BE32 model [21] implemented in PYTHIA. Only BEC between hadrons originating from the same W boson are taken into account, as suggested by our measurements [22]. Colour-Reconnection (CR) effects [23] in the qqqq final state would alter the colour flow between the W bosons. In accordance with our measurement [24], these are not implemented in the Monte Carlo simulation. However, both the effect of BEC between hadrons originating from different W decays and that of CR between W bosons are considered as possible systematic uncertainties.

The response of the L3 detector is modelled with the GEANT [25] program which includes the effects of energy loss, multiple scattering and showering in the detector material. Hadronic showers are simulated with the GHEISHA [26] program. Time-dependent detector efficiencies, as monitored during data taking, are included in the simulation.

4 Event reconstruction

In the qqeν, qq$\mu\nu$ and qqqq channels a kinematic fit is applied to improve the resolution of the measured energies, E_f, momenta, p_f, polar, θ_f, and azimuthal, ϕ_f, angles of the visible fermions. Four-momentum conservation and other constraints, as detailed below, are imposed. The measured quantities are varied within their resolution to satisfy these constraints. The resolution of each individually-measured object depends on details of the reconstruction, such as the detector region or the energy scale. The average resolutions of E_f, θ_f, and ϕ_f for electrons, muons and hadronic jets, as determined by Monte Carlo simulation, are given in Table 2. These values agree with the resolutions derived from calibration data collected at the Z resonance within the statistical accuracy of the test.

In all events, four-momentum conservation is required which, in the case of the qqeν and qq$\mu\nu$ final states, determines the momentum and the direction of the neutrino. For hadronic jets, the velocity $\beta_f = p_f/E_f$ is fixed to its measured value, as many systematic effects cancel in this ratio. When imposing energy conservation, the $\sqrt{s}$ value determined for each event by the LEP Energy Working Group [27] is used. Events collected during the manipulation of the LEP beams, for which no precise calibration of the LEP energy is available, are excluded from the analysis. Energy conservation results in a one-constraint (1C) kinematic fit for qqeν and qq$\mu\nu$ final states and a four-constraint (4C) kinematic fit for the qqqq channel. In general, fermion angles are better measured than energies and momenta. Therefore, the kinematic fit improves more the determination of the latter. The improvement in the resolution of the average value of the two reconstructed W-boson masses is shown in Table 3.

In the 1C and 4C fits, the masses of the two W bosons are determined separately. The mass resolution is further improved by the additional constraint of requiring these masses to be equal within the width of the W boson, fixed as 2.1 GeV. This numerical value does not bias the resulting fits. This procedure results in a two-constraint (2C) fit of qqeν and qq$\mu\nu$ events and a five-constraint (5C) fit of qqqq events. For qqeν and qq$\mu\nu$ events, both the mass of the hadronically-decaying W boson obtained in the 1C fit, $m_{1\mathrm{C}}$, and the average mass obtained in the 2C fit, $m_{2\mathrm{C}}$, are used in the mass extraction, which is described in the following section. Similarly, in the qqqq channel, the average masses of the 4C fit, $m_{4\mathrm{C}}$, and the 5C fit, $m_{5\mathrm{C}}$, are used.

The qq$\tau\nu$ final state contains at least two neutrinos and only the W boson decaying into hadrons is used in the mass reconstruction. The energies of the two hadronic jets are rescaled by a common factor such that the sum of their energies equals $\sqrt{s}/2$, effectively imposing an equal-mass constraint on the two W bosons. Use of the mass of the hadronic system after this rescaling, m_{resc}, improves the resolution of the W-boson mass reconstruction by more than a factor of two.

The improvement of the mass resolution due to the kinematic fit is shown in Figure 1. The average mass resolutions before and after the kinematic fits or the energy rescaling is summarised in Table 3 for all final states. Only the better-measured quantities $m_{2\mathrm{C}}$ and $m_{5\mathrm{C}}$ are used to determine Γ_{W}.

W-boson pair production is frequently accompanied by photon radiation. Photons near to a final-state fermion are mainly due to final-state radiation (FSR). In qqeν events, photons close to the electron are automatically included into the measurement of the electromagnetic cluster. In qq$\mu\nu$ events, the cluster closest to the muon direction is assumed to originate from the ionisation energy loss of the muon in the calorimeters and is taken out of the event. In qq$\tau\nu$ events, the photon clusters are combined in the tau jet by the jet-reconstruction cone algorithm. Hard photons with energies greater than 5 GeV and outside a cone of 5° half-opening angle around the lepton are detected in 5% of the qqeν events and in 2.5% of the qq$\mu\nu$ events. They are taken into account by the kinematic fit, but not incorporated in the mass reconstruction, as they are mainly due to initial-state radiation (ISR). In all other cases, the detected photons are assigned to the jets during the clustering process. For photons emitted along the beam direction, and therefore undetected, the analysis relies on the Monte Carlo simulation.

Systematic uncertainties arise in the qqqq channel due to potential effects of CR between the jets from different W bosons. To reduce these effects, clusters with an energy below 2 GeV are removed from the original jets obtained by the jet clustering process, as discussed in Section 6.9. The jet energies and momenta are re-scaled with an equal scale factor in order to obtain the original jet energy. Only the jet directions and the jet masses are affected by this

procedure and the energy resolution of the jets is preserved as illustrated in Table 2. On the other hand, the angular resolution of the jets is worsened leading to a degradation of the W-boson mass resolution by about 20%. The resulting increase of the statistical uncertainty on m_{W} is overcompensated by a reduction of the systematic uncertainty, leading to a lower total uncertainty, as discussed in Section 6.9.

The mass resolution in the fully-hadronic final state is improved by taking into account gluon radiation from quarks. The DURHAM jet-resolution parameter for which the event topology changes from four to five jets, y_{45}, is used to separate events with and without gluon radiation. Those with $\log y_{45} > -6.2$ are treated as four-jet events and the remaining as five-jet events.

The four or five jets must be associated with the two W bosons. In the case of four jets, all three combinations are considered. Five jets can be paired in ten different ways. Monte Carlo studies show that in five-jet events only some combinations have a high probability to be correct. These are the ones in which the W boson that decays without hard-gluon radiation is formed by the highest-energy jet and any other jet or by the second highest-energy jet and any other jet except the lowest-energy jet. Only these six combinations are considered. The three pairings with the highest kinematic-fit probability are retained. They are ordered by their fit probability and treated as separate samples. Pairings where the fit did not converge are rejected. This criterion removes 5% of the events.

The four-jet and five-jet samples, of about equal size, are treated in separate mass fits since their mass resolutions are different by about 30% as shown in Table 3. Due to the overall improvement in mass resolution, the statistical uncertainty of m_{W}, as determined in the fully-hadronic channel, is reduced by 6%.

The mass spectra after the kinematic fit for the better-measured mass variable m_1 are shown in Figure 2 for the semi-leptonic final states and the best pairing in the fully-hadronic final state. Figure 3 presents the sum of the semi-leptonic distributions, while Figure 4 shows the sum of all four distributions.

5 Extraction of m_{W} and Γ_{W}

A maximum-likelihood method is used to extract m_{W} and Γ_{W} from the reconstructed masses of each event. The extraction of m_{W} and Γ_{W} is done separately for each of the four final states, qqeν, qq$\mu\nu$, qq$\tau\nu$ and qqqq, and the seven average values of $\sqrt{s}$. For each of these 28 event samples a likelihood function, $L(m_{\mathrm{W}}^{\mathrm{fit}}, \Gamma_{\mathrm{W}}^{\mathrm{fit}})$, is constructed from the product of the individual likelihoods. These are evaluated for each mass reconstruction, i, performed for a given semi-leptonic event or a given pairing of the four- and five-jet samples of the fully-hadronic final state. Correlations between the reconstructed masses from different pairings are found to be negligible. The individual likelihoods are calculated from the normalised differential cross sections in terms of the reconstructed masses, m_1 and m_2,

$$L(m_{\mathrm{W}}^{\mathrm{fit}}, \Gamma_{\mathrm{W}}^{\mathrm{fit}}) \;=\; \prod_i \frac{f(m_{\mathrm{W}}^{\mathrm{fit}}, \Gamma_{\mathrm{W}}^{\mathrm{fit}}) \left(\dfrac{\mathrm{d}^2\sigma(m_{\mathrm{W}}^{\mathrm{fit}}, \Gamma_{\mathrm{W}}^{\mathrm{fit}})}{\mathrm{d}m_1\,\mathrm{d}m_2}\right)_i + \left(\dfrac{\mathrm{d}^2\sigma_{\mathrm{back}}}{\mathrm{d}m_1\,\mathrm{d}m_2}\right)_i}{f(m_{\mathrm{W}}^{\mathrm{fit}}, \Gamma_{\mathrm{W}}^{\mathrm{fit}})\,\sigma(m_{\mathrm{W}}^{\mathrm{fit}}, \Gamma_{\mathrm{W}}^{\mathrm{fit}}) + \sigma_{\mathrm{back}}}\,, \qquad (1)$$

where σ and σ_{back} are the accepted signal and background cross sections of the corresponding final state. As summarised in Table 3, the masses are chosen as $m_1 = m_{2\mathrm{C}}$ and $m_2 = m_{1\mathrm{C}}$ for qq$\mu\nu$ and qqeν final states and $m_1 = m_{5\mathrm{C}}$ and $m_2 = m_{4\mathrm{C}}$ for fully-hadronic events. For qq$\tau\nu$ events the doubly-differential cross section is reduced to a singly-differential one and only the

rescaled mass of the hadronic system is used, $m_1 = m_{\rm resc}$. The normalisation factor $f(m_{\rm W}^{\rm fit}, \Gamma_{\rm W}^{\rm fit})$ is calculated such that the sum of the accepted background and the reweighted signal cross section reproduces the measured cross section. This procedure determines $m_{\rm W}$ and $\Gamma_{\rm W}$ solely from the shapes of the mass distributions. In the fits to determine $m_{\rm W}$, the Standard Model relation $\Gamma_{\rm W} = 3G_{\rm F}m_{\rm W}^3(1 + 2\alpha_{\rm s}/3\pi)/(2\sqrt{2}\pi)$ is imposed [28]. When $\Gamma_{\rm W}$ is extracted, $m_{\rm W}$ and $\Gamma_{\rm W}$ are treated as independent quantities and the doubly-differential cross section is reduced to a single one, since only the better-measured quantity m_1 is used for the determination of $\Gamma_{\rm W}$.

The total and differential cross sections of signal and background accepted by the event selection are determined using Monte Carlo simulations. Except for single-W production, the background cross sections are independent of $m_{\rm W}$ and $\Gamma_{\rm W}$. The signal Monte Carlo simulation, which is originally generated using a particular value of the W-boson mass, $m_{\rm W}^{\rm gen}$, and width, $\Gamma_{\rm W}^{\rm gen}$, is modified in a reweighting procedure to represent a different W-boson mass, $m_{\rm W}^{\rm fit}$, and width, $\Gamma_{\rm W}^{\rm fit}$. Each signal Monte Carlo event, j, is given a new weight, R_j, defined by the ratio

$$R_j(m_{\rm W}^{\rm fit}, \Gamma_{\rm W}^{\rm fit}, m_{\rm W}^{\rm gen}, \Gamma_{\rm W}^{\rm gen}) \;=\; \frac{\left|\mathcal{M}(p_j^1, p_j^2, p_j^3, p_j^4, k_j^\gamma, m_{\rm W}^{\rm fit}, \Gamma_{\rm W}^{\rm fit})\right|^2}{\left|\mathcal{M}(p_j^1, p_j^2, p_j^3, p_j^4, k_j^\gamma, m_{\rm W}^{\rm gen}, \Gamma_{\rm W}^{\rm gen})\right|^2}\,, \tag{2}$$

where $\mathcal{M}$ is the matrix element of the four-fermion final state under consideration. The matrix elements are calculated for the generated four-vectors of the four fermions, $p_j^{n=1\ldots4}$ using the program EXCALIBUR [29]. Since this program is based on four-fermion final states without additional photons, the momentum sum of any ISR photons present in the Monte Carlo events, k_j^γ, is taken into account by boosting the four fermions into the rest frame of the event after the ISR photon emission. Photons not emitted in the initial state are recombined with the closest final-state fermion. It was verified that this method is equivalent to using the KANDY program, which simulates photon radiation in the event generation. As a cross check of the matrix element reweighting the event weights are evaluated from a Breit-Wigner function. Consistent results are observed.

The total accepted signal cross section for a given set of parameters, $m_{\rm W}^{\rm fit}$ and $\Gamma_{\rm W}^{\rm fit}$, is

$$\sigma(m_{\rm W}^{\rm fit}, \Gamma_{\rm W}^{\rm fit}) \;=\; \frac{\sigma^{\rm gen}}{N^{\rm gen}} \sum_j R_j(m_{\rm W}^{\rm fit}, \Gamma_{\rm W}^{\rm fit}, m_{\rm W}^{\rm gen}, \Gamma_{\rm W}^{\rm gen})\,, \tag{3}$$

where $\sigma^{\rm gen}$ denotes the cross section corresponding to the total Monte Carlo sample containing $N^{\rm gen}$ events. The sum extends over all Monte Carlo events, j, accepted by the event selection. The total background cross section is

$$\sigma_{\rm back} \;=\; \sum_l \frac{\sigma_{{\rm back},l}^{\rm gen}}{N_{{\rm back},l}^{\rm gen}}\, N_{{\rm back},l}^{\rm sel}\,, \tag{4}$$

where, for each background process l with generated cross section $\sigma_{{\rm back},l}^{\rm gen}$, $N_{{\rm back},l}^{\rm gen}$ and $N_{{\rm back},l}^{\rm sel}$ are the numbers of generated and accepted Monte Carlo events, respectively.

To determine the accepted differential cross section for a given data event, i, the box method [30] is applied. When combined with the reweighting procedure, this method takes into account detector and selection effects, efficiencies and purities which depend on $m_{\rm W}$ and $\Gamma_{\rm W}$ and correlations between the input masses m_1 and m_2. The accepted differential cross section is determined by averaging signal Monte Carlo events inside a two-dimensional mass domain, Ω_i, centred around each data event. To take the different resolutions of m_1 and m_2 into account, these masses are rescaled by their resolutions σ_1 and σ_2 whose averages are given

in Table 3. The size of each domain is limited by requiring a sufficient number of Monte Carlo events in the domain. In the rescaled parameter space, the distance, d_{ij}, of each Monte Carlo event, j, from the given data event, i, with reconstructed masses $(m_1)_i$ and $(m_2)_i$ is calculated from

$$d_{ij} = \sqrt{\left(\frac{(m_1)_j - (m_1)_i}{\sigma_1}\right)^2 + \left(\frac{(m_2)_j - (m_2)_i}{\sigma_2}\right)^2} , \tag{5}$$

and the 400 closest Monte Carlo events are retained.

The most distant Monte Carlo event, $j_{\max}$, determines the mass intervals around the data event, $(\delta m_1)_i = |(m_1)_i - (m_1)_{j_{\max}}|$ and $(\delta m_2)_i = |(m_2)_i - (m_2)_{j_{\max}}|$, which vary between 200 MeV and 600 MeV. After summing the weights R_j of all Monte Carlo events associated to the mass domain Ω_i around the considered data event, the differential cross section of the signal processes is given by

$$\left(\frac{\mathrm{d}^2\sigma(m_{\mathrm{W}}^{\mathrm{fit}}, \Gamma_{\mathrm{W}}^{\mathrm{fit}})}{\mathrm{d}m_1\, \mathrm{d}m_2}\right)_i = \frac{1}{\pi(\delta m_1)_i(\delta m_2)_i} \frac{\sigma^{\mathrm{gen}}}{N^{\mathrm{gen}}} \sum_{j\in\Omega_i} R_j(m_{\mathrm{W}}^{\mathrm{fit}}, \Gamma_{\mathrm{W}}^{\mathrm{fit}}, m_{\mathrm{W}}^{\mathrm{gen}}, \Gamma_{\mathrm{W}}^{\mathrm{gen}}) . \tag{6}$$

For the background Monte Carlo simulation, the same domain size as for the signal is chosen and the differential distribution of the background is determined from the number of selected background Monte Carlo events, $(N_{\mathrm{back}}^{\mathrm{sel}})_i$, associated with a given data event:

$$\left(\frac{\mathrm{d}^2\sigma_{\mathrm{back}}}{\mathrm{d}m_1\, \mathrm{d}m_2}\right)_i = \frac{1}{\pi(\delta m_1)_i(\delta m_2)_i} \frac{\sigma_{\mathrm{back}}^{\mathrm{gen}}}{N_{\mathrm{back}}^{\mathrm{gen}}} (N_{\mathrm{back}}^{\mathrm{sel}})_i . \tag{7}$$

One-dimensional boxes in the m_1 space are constructed for the determination of Γ_{W}. The size of each bin is defined by requiring at least 200, but not more than 1000, Monte Carlo events. The bin size is at most ± 250 MeV around $(m_1)_i$ and decreases to about ± 30 MeV around the peak of the mass spectrum. For the background Monte Carlo simulation, the bin size is chosen as ± 1 GeV around $(m_1)_i$.

6 Systematic uncertainties

The systematic uncertainties on m_{W} and Γ_{W} are summarised in Tables 4 and 5, respectively. They arise from various sources correlated or un-correlated between the final states and between the various $\sqrt{s}$ values. The different sources of the systematic uncertainty are detailed in the following subsections and their correlations are discussed in Section 7.

Systematic uncertainties are assessed by determining Δm_{W} and $\Delta\Gamma_{\mathrm{W}}$ which are defined as the changes of the m_{W} and Γ_{W} results if alternative detector calibrations, Monte Carlo simulations or reconstruction procedures are used. Two methods are used for the evaluation of Δm_{W}. In the cases where the effect of an alternative Monte Carlo simulation is studied, the usual mass fit is used, but the data events are replaced by a high-statistics sample from the alternative simulation. The fit result, $m_{\mathrm{W}}^{\mathrm{fit}}$, is compared to the nominal W-boson mass common to both Monte Carlo samples, $m_{\mathrm{W}}^{\mathrm{gen}}$, deriving $\Delta m_{\mathrm{W}} = m_{\mathrm{W}}^{\mathrm{gen}} - m_{\mathrm{W}}^{\mathrm{fit}}$. A similar procedure is used to derive $\Delta\Gamma_{\mathrm{W}}$. In the cases where the agreement between data and simulation is analysed, the shift of the reconstructed mass is calculated for each data and Monte Carlo event. The average mass shifts of the data and Monte Carlo distributions are compared to determine Δm_{W}.

6.1 Calibration of $\sqrt{s}$

The value of $\sqrt{s}$ is used as a constraint in the kinematic fit. A variation of $\sqrt{s}$ would imply a shift of the reconstructed masses. The relative uncertainty on m_{W} is the same as that on $\sqrt{s}$, while Γ_{W} is less affected. This is verified by comparing simulated event samples in which the $\sqrt{s}$ value used in the kinematic fit is systematically changed. The dependences of m_{W} and Γ_{W} on $\sqrt{s}$ are taken into account using the LEP energy determined for the exact time each W-boson pair was recorded. The LEP beam energy is known with an accuracy between 10 and 20 MeV [27]. The complete error matrix from Reference 27 is used to determine the uncertainties on m_{W} and Γ_{W} given in Tables 4 and 5, which are correlated between all final states.

As a cross check of the $\sqrt{s}$ calibration, events from the $\mathrm{e^+e^-} \to \mathrm{Z}\gamma$ process with hard ISR were used to measure the mass of the Z boson [31]. The Z-boson mass, m_{Z}, was determined to be $91.272 \pm 0.032 \pm 0.033$ GeV, where the first uncertainty is statistical and the second systematic, in agreement with the value measured at the Z resonance [32], $m_{\mathrm{Z}} = 91.190 \pm 0.003$ GeV. Assuming this value of m_{Z}, the method determines the average $\sqrt{s}$ to be $175 \pm 68 \pm 68$ MeV lower than the value given by the LEP energy calibration, but consistent within the experimental uncertainty.

The intrinsic energy spread of the beams causes a $\sqrt{s}$ distribution of the individual events with a Gaussian width of 240 MeV. To assess this effect, the $\sqrt{s}$ constraint in the Monte Carlo events is varied by the same amount. The changes of m_{W} and Γ_{W} are negligible.

6.2 Lepton measurement

The measurement of the lepton energy in $\mathrm{qqe}\nu$ and $\mathrm{qq}\mu\nu$ events affects the mass reconstruction, while in the $\mathrm{qq}\tau\nu$ final state it is solely based on the measurement of the jets. Control samples of events from the $\mathrm{e^+e^-} \to \ell^+\ell^-$ process are selected in calibration runs at the Z resonance and are used to cross check lepton reconstruction. The absolute energy scales for electrons and muons are known with a precision of 50 MeV. Varying the lepton energy scale by this amount and increasing the lepton energy resolution in the simulation by 25% of the value measured with Z-resonance data, results in the changes of m_{W} and Γ_{W} detailed in Table 6. Effects due to the determination of the lepton angles are negligible.

The distributions of the energy of calorimetric clusters around the charged lepton are shown in Figure 5a and 5b. These clusters are normally joined to one of the jets. If they are not correctly described by the Monte Carlo simulation, this might result in a bias on the value of m_{W}. To assess this effect, all clusters within a cone of 5° half-opening angle around the lepton are excluded from the jets. No significant effect on m_{W} is observed.

6.3 Jet measurement

The measurements of jet energies and directions affect the mass spectra and are a potential source of systematic uncertainties on m_{W} and Γ_{W}. These uncertainties are assigned by varying the jet-energy scale by 50 MeV, smearing the jet energies by 1% and smearing the jet directions by 0.5°. The sizes of these variations correspond to the uncertainties estimated from $\mathrm{e^+e^-} \to \mathrm{qq}$ events collected in calibration runs at the Z resonance. These variations are applied to the Monte Carlo sample taken as reference to extract m_{W} and Γ_{W} from the data. The effects on m_{W} and Γ_{W} are given in Table 6. As expected, the largest effect appears in the $\mathrm{qq}\tau\nu$ channel, where only the rescaled jets are used and no additional constraint is applied.

Generally, the event primary-vertex is shifted with respect to the geometrical centre of the detector. If this shift was left uncorrected, it would imply a systematic distortion of the jet angles. The actual position of the primary vertex is measured using data and corrected for in the reconstruction procedure. The shift is found to be less than 4 mm along the beam axis and 0.5 mm in the transverse plane, with an uncertainty of less than 5%. Figure 6a shows for each data event the shift of the reconstructed mass due to the vertex correction. Assuming that the vertex is displaced within the uncertainty of its determination results in a change of m_{W} of less than 1 MeV.

Deviations of the calorimeter positions from their nominal locations would also cause angular distortions. To check the angular measurement of the calorimetric clusters the measurement of m_{W} is repeated using only clusters associated with tracks. For each event, the mass is first reconstructed using the angular information of the clusters and then from the angles of the associated tracks. These measurements are independent. The resulting mass-shift distribution is shown in Figure 6b. Combining all final states we obtain a change of m_{W} of -1 ± 9 MeV between both methods, consistent with zero.

Angle-dependent effects in the energy scale of the calorimeters could lead to an additional bias in the measurement of the jet angles. For instance, if forward clusters had a relative bias towards lower energy than clusters in the central part of the detector, the direction of the jet would be shifted towards the central detector region. This effect is expected to be most evident in the qqqq events, which are strongly constrained by the kinematic fit. To assess this effect the raw jet energies are compared to the jet energies after the kinematic fit for various polar-angle regions of the detector. No significant change in m_{W} is observed if the cluster-energy scale in the simulation is changed for each polar-angle region to agree exactly with the data.

The energy spectrum of the clusters and the energy flow with respect to the jet axis are also investigated. They are shown in Figures 7a and 8a, respectively. Figures 7b and 7c present the effect on m_{W} when clusters below a given energy cut are removed. The changes of m_{W} stay within the statistical uncertainty of the test when varying the energy cut from the default values of 100 MeV and 2 GeV for $\mathrm{qq}\ell\nu$ and qqqq events, respectively. No significant change of m_{W} is observed if clusters outside a cone around the jet axis are removed, as shown in Figures 8b and 8c for cones of half-opening angles from 30° to 180°.

6.4 Fit procedure

The fit procedure determines m_{W} and Γ_{W} without any bias as long as the Monte Carlo simulation correctly describes effects such as photon radiation and detector resolution. This fit procedure is tested to high accuracy by fitting large Monte Carlo samples, typically a hundred times the size of the data sample. The fits reproduce well the generated values $m_{\mathrm{W}}^{\mathrm{gen}}$ and $\Gamma_{\mathrm{W}}^{\mathrm{gen}}$ within the statistical accuracy of the test, over a range of $\pm$500 MeV in m_{W} and $\pm$600 MeV in Γ_{W}.

In the fit of m_{W} the number of events per box is varied between 350 and 450, while in the fit of Γ_{W} the minimal number of events is varied between 150 and 250. In addition, the fit is restricted to masses in the range between 70 GeV and 90 GeV. No statistically significant effect on m_{W} or Γ_{W} is observed for any of these variations.

The reliability of the uncertainties given by the fit is tested by fitting for each final state several hundred small Monte Carlo samples, each the size of the data sample. The width of the distribution of the fitted central values agrees well with the mean of the distribution of the fit uncertainties.

6.5 Background

Background which is not correctly described by the Monte Carlo simulation, either in the total number of events or in their mass distribution, could cause a shift of m_{W} and Γ_{W}. For both the semi-leptonic and the fully-hadronic selections, the four-fermion background is scaled by $\pm 5\%$. Additionally, background from the $\mathrm{e^+e^-} \to \mathrm{qq}$ process is scaled by $\pm 5\%$ and the slope of its mass spectrum is varied by $\pm 10\%$ over the mass range between 65 GeV and 95 GeV.

The dominant background in the fully-hadronic selection is due to $\mathrm{e^+e^-} \to \mathrm{qq}$ events with multiple gluon radiation. To better reproduce the four-jet rate observed in hadronic Z decays, a reweighting of the $\mathrm{e^+e^-} \to \mathrm{qq}$ Monte Carlo events according to the value of y_{34} is applied in our standard mass-extraction procedure [12]. Removing this reweighting changes the total background contribution by 12% and shifts m_{W} and Γ_{W} by 10 MeV and 80 MeV, respectively. Half of the shift is taken as systematic uncertainty.

The effects on m_{W} and Γ_{W} due to the variation of height and slope of the background mass spectrum and the uncertainty due to the reweighting of the y_{34} spectrum are summarised in Table 7. The individual sources are added in quadrature to yield the systematic uncertainty due to the background simulation.

6.6 Monte Carlo statistics

The systematic uncertainty due to the limited size of the signal Monte Carlo sample used for the box fit is estimated by dividing it into several sub-samples of equal size and using each of them to fit the data. The systematic uncertainty due to Monte Carlo statistics is then determined by extrapolating the spread of the fit results to the full Monte Carlo sample. The total systematic uncertainties on m_{W} and Γ_{W} due to limited Monte Carlo statistics are given for each final state in Tables 4 and 5, respectively.

6.7 Photon radiation

Four-fermion production, including its radiative corrections, is modelled by the KANDY and RACOONWW Monte Carlo generators. Both programs use pole expansions [33] for the calculation of $\mathcal{O}(\alpha)$ corrections. KANDY models ISR using the Yennie-Frautschi-Suura (YFS) exponentiation scheme [34], while FSR is simulated by the program PHOTOS [35] in the case of charged leptons and by PYTHIA in the case of quarks. Interference between ISR and FSR is neglected. RACOONWW implements the full $\mathcal{O}(\alpha)$ matrix element for the radiative four-fermion production, $\mathrm{e^+e^-} \to ffff\gamma$. Higher-order corrections coming from multiple ISR photons are implemented using a structure-function ansatz. As the calculations implemented in RACOONWW are based on massless fermions, the FSR simulation exhibits a minimum cut-off on the photon-fermion angle.

The radiation of hard and isolated photons is better simulated by RACOONWW which implements the complete matrix element of the $ffff\gamma$ final state. On the other hand, soft and collinear photons are not generated, which makes the KANDY approach more appropriate for comparison with data. KANDY uses a W propagator with a mass-dependent term containing the W width, whereas RACOONWW uses a constant term. Because the definitions differ by 27 MeV in the position of the W peak [36], the $m_{\mathrm{W}}^{\mathrm{gen}}$ input to RACOONWW is chosen 27 MeV lower than for KANDY in order to give an identical W-boson lineshape.

A total of 300 000 Monte Carlo events of the qqeν, qq$\mu\nu$ and qqqq final states are generated with the RACOONWW program at $\sqrt{s} = 207$ GeV, including full detector simulation. Events

with hard-photon radiation are selected at the generator level using the CALO5 algorithm [37], which recombines soft and collinear photons with the nearest fermion. These events, after detector simulation, are used instead of data in the mass fit which relies on KANDY as the reference Monte Carlo. The change in m_{W} from the comparison of the programs is derived and scaled by the fraction of events with hard-photon radiation, which is of the order of 10%. The same effect as observed in the $\mathrm{qq}\mu\nu$ channel is assumed for the $\mathrm{qq}\tau\nu$ channel where no events were generated. In an additional test, the KANDY events are reweighted such that they represent the $\mathcal{O}(\alpha^2)$ ISR corrections instead of the $\mathcal{O}(\alpha^3)$ calculation. The changes of m_{W} and Γ_{W} resulting from these tests are detailed in Table 8. For each final state they are added in quadrature to estimate the systematic uncertainties on m_{W} and Γ_{W} due to the modelling of photon radiation, given in Tables 4 and 5.

6.8 Hadronisation

The hadronisation process is modelled by three different schemes as implemented in the Monte Carlo programs PYTHIA, HERWIG and ARIADNE. For the perturbative phase PYTHIA and HERWIG simulate a parton shower, while a dipole cascade is produced in ARIADNE. The Lund string-hadronisation model is used by PYTHIA and ARIADNE, while HERWIG employs a cluster model. A comparison of the mass distributions of the three different models with data is shown in Figure 9. Within the statistical accuracy, all three Monte Carlo distributions are compatible with the data.

The results for m_{W} and Γ_{W} presented in this paper are based on the PYTHIA model. Systematic effects due to modelling of the hadronisation process are determined by comparison with the other two programs. In the mass-extraction fit the data events are replaced by high-statistics samples of Monte Carlo events generated with PYTHIA, HERWIG and ARIADNE. These Monte Carlo samples consist of events which are identical at the four-fermion level and thus differ only in their hadronisation. The changes of m_{W} and Γ_{W} due to the use of HERWIG or ARIADNE are listed in Table 9. For m_{W}, HERWIG and ARIADNE reproduce the PYTHIA results within the statistical uncertainty, except in the $\mathrm{qq}\tau\nu$ channel. This is mainly caused by the misassignment of energy deposits from the remainder of the event to the tau-lepton jet which is based on a cone definition. This effect, altering the reconstruction of the jets and therefore m_{W}, strongly depends on the choice of the hadronisation model. For Γ_{W}, ARIADNE is in good agreement with PYTHIA, while HERWIG shows significant differences, especially for semi-leptonic final states.

The four-momenta of calorimetric clusters which are used to form hadronic jets are calculated using the energy and angle measurements and assuming their masses to be either zero or the pion mass. However, kaons and protons are frequently produced resulting in a shift of the jet masses. This shift is automatically corrected in the mass-extraction fit which uses the Monte Carlo simulation containing these hadrons. If the simulation predicts different multiplicities for these heavier hadrons than is present in data, systematic effects on the measurement of m_{W} and Γ_{W} are expected. In order to assess this systematic effect, the mean number of charged kaons and protons produced in the W-boson decays of our simulation is compared to measurements [38] and found to be in agreement. The shifts Δm_{W} and $\Delta\Gamma_{\mathrm{W}}$ are calculated with Monte Carlo events reweighted such that the mean kaon and proton multiplicities agree exactly with the measured values. It is checked that the mass spectrum at generator level is not distorted by this reweighting procedure. Figure 10 shows the linear dependence of Δm_{W} on the average kaon and proton multiplicity. This linear dependence is used to translate the

uncertainty of the measured kaon and proton multiplicities into uncertainties on m_{W} and Γ_{W}. Table 10 presents the shifts and uncertainties of m_{W} and Γ_{W} due to the correction of the Monte Carlo simulation.

In the qqqq final state, the DURHAM parameter y_{45} is used to discriminate events with hard-gluon radiation. This variable might be affected by hadronisation uncertainties. A change of the selection criterion $\log y_{45} < -6.2$ between -5.8 and -6.6 has no significant influence on m_{W}.

The average absolute shift of m_{W} and Γ_{W} due to the alternative hadronisation models ARIADNE and HERWIG and the uncertainty deduced from the variation of the kaon and proton multiplicities in the Monte Carlo simulation are added in quadrature to yield the total uncertainties due to the hadronisation modelling, given in Tables 4 and 5.

6.9 Final state interactions in fully-hadronic events

The Monte Carlo programs hadronise the quarks from the two W bosons independently. However, CR effects would invalidate this assumption and thus affect the mass reconstruction. Similarly, BEC between bosons arising from different W bosons, if incorrectly modelled, could have the same effect.

Our measurements [22,39,40] of BEC indicate that correlations in hadronic W-boson decays are very similar to those in Z-boson decays into light quarks. Furthermore, BEC between hadrons from different W bosons are disfavoured. They are limited to at most 30% of the strength simulated in the BE32 model [21] implemented in PYTHIA 5.7. Since all our previous mass measurements at $\sqrt{s} = 172 - 183$ GeV were performed under the assumption of full inter-W BEC, the results obtained in the qqqq channel are re-evaluated in light of our measurement of vanishing inter-W BEC.

Reference 22 presents the L3 measurement of the difference between the two-particle densities of the data and the simulation without inter-W BEC, $\Delta\rho_2(Q)$. The integral, J, of this difference is measured to be below 0.39 at 68% confidence level. For different Monte Carlo samples, generated with various strengths of inter-W BEC, but fixed strength of the intra-W BEC, the integral J is determined. The shift Δm_{W} exhibits a linear dependence with respect to J, as shown in Figure 11. The effects on m_{W} and Γ_{W} for a maximum inter-W BEC, as allowed by our direct BEC measurement, are detailed in Table 11. A linear dependence of BEC effects on $\sqrt{s}$ is assumed.

A dedicated study of reconnection effects in the particle flow between jets in qqqq events shows that the data are consistent with no or only a small CR effect [24]. A 68% upper limit on the CR parameter k_I is set at 1.1 in the framework of the SK-I model [41] as implemented in PYTHIA 5.7. The influence of the CR parameter k_{I} on m_{W} is studied in the SK-I framework by mixing event samples simulated at $\sqrt{s} = 189$ GeV with full and without inter-W CR. The result is shown in Figure 12 for moderate values of k_{I} where a linear dependence can be assumed. The particle flow analysis is found to be insensitive to CR effects implemented in other models such as ARIADNE type II [42] and HERWIG [43]. The ARIADNE-II model is compared to the ARIADNE-I model, the latter having been modified such that in both models the shower cascade is performed in two phases with an identical cut-off parameter.

These Monte Carlo studies show that the effect of CR on m_{W} grows with increasing $\sqrt{s}$ in the case of the SK-I model, while only little dependence on $\sqrt{s}$ is seen for ARIADNE and HERWIG. For all energies and all models the shift of m_{W} is comparable or smaller than the shift predicted by the SK-I model at $k_{\mathrm{I}} = 1.1$, which is used to estimate the systematic uncertainty

due to CR effects. It is interesting to note that studies of the distribution of particles in the inter-jet region of three-jet hadronic Z decays exclude the predictions of the CR models of ARIADNE and HERWIG for this case [44]. No version of the SK-I model applicable to Z decays exists.

The use of a cone algorithm for jet clustering lowers the sensitivity to CR effects, as the analysis is less affected by the inter-jet regions where the influence of CR is largest. More effectively, removing clusters below a certain energy cut rejects particles predominantly produced during the non-perturbative phase of the hadronisation process where CR effects take place. Monte Carlo studies are performed at $\sqrt{s} = 189$ GeV applying various cuts on the minimum cluster energy. The dependence of the m_{W} shift on the energy cut is extrapolated to the full data sample and shown in Figure 13. The additional component to the statistical uncertainty due to the slight degradation of the mass resolution caused by the cut is calculated and added in quadrature to the shift of m_{W}. A cut at minimum cluster energies of 2 GeV is found to be the optimal choice and is therefore used in the extraction of m_{W} and Γ_{W} from the data of the qqqq final state. Table 12 presents the effect of CR on m_{W} and Γ_{W}.

Monte Carlo studies show that the relative reduction of the m_{W} shift due to the energy cut is independent of k_{I} and $\sqrt{s}$. The mass shifts observed for the SK-I Monte Carlo simulation with full CR at various $\sqrt{s}$ values are obtained using the dependence on k_{I} and on the energy cut extracted at $\sqrt{s} = 189$ GeV. The systematic uncertainties on m_{W} are calculated using a linear dependence on $\sqrt{s}$ and assumed to be fully correlated. For Γ_{W} no $\sqrt{s}$ dependence is seen.

7 Results

Figure 14 compares the m_{W} measurements in the four different final states at the seven average $\sqrt{s}$ values. The measurements of m_{W} and Γ_{W} from the individual final states are combined using the "best linear unbiased estimate" technique [45]. This combination method takes into account all systematic uncertainties as well as their correlations. When combining measurements taken at different $\sqrt{s}$ values, the correlations of the LEP energy determination [27] are used. Within each final state, the uncertainties due to lepton measurement, background determination, BEC and CR are taken as fully correlated between the measurements at different $\sqrt{s}$. The uncertainties due to jet measurement, photon radiation and hadronisation are fully correlated between all final states and between all $\sqrt{s}$ values. The systematic uncertainty due to limited Monte Carlo statistics remains uncorrelated for all measurements. In the case of the simultaneous estimate of m_{W} and Γ_{W}, the correlations between both parameters as determined in the individual box fits are included in the combination procedure.

Combined results of m_{W} are shown in Figure 15 for each $\sqrt{s}$ value averaged over the final states. Figure 16 shows the results for each final state and their combination. Table 13 gives the results on m_{W} for each final state. The combination of the results at $\sqrt{s} = 189 - 209$ GeV yields for the semi-leptonic and the fully-hadronic final states:

$$m_{\mathrm{W}}(\mathrm{qq}\ell\nu) = 80.196 \pm 0.070 \pm 0.026 \text{ GeV} \quad \text{and} \tag{8}$$

$$m_{\mathrm{W}}(\mathrm{qqqq}) = 80.298 \pm 0.064 \pm 0.049 \text{ GeV} \quad . \tag{9}$$

Here and in the following, the first uncertainty is statistical and the second systematic. The $\mathrm{qq}\ell\nu$ and the qqqq channels exhibit a correlation of 9%. The contributions of the individual sources of systematic uncertainty to the combined m_{W} value in the $\mathrm{qq}\ell\nu$ channel is given in Table 4.

The difference between the values of m_{W} determined in the qq$\ell\nu$ and qqqq channels is

$$m_{\mathrm{W}}(\mathrm{qq}\ell\nu) - m_{\mathrm{W}}(\mathrm{qqqq}) \;=\; -0.088 \pm 0.094 \pm 0.031 \text{ GeV} . \tag{10}$$

BEC and CR effects are not included in the systematic uncertainty on the mass difference. Moreover, hadronisation uncertainties are treated as uncorrelated between the qq$\ell\nu$ and qqqq final states. This causes the mass difference not to equal the difference of the mass values given in Equations (8) and (9).

Averaging the values of the qq$\ell\nu$ and qqqq channels, including BEC and CR uncertainties and all correlations, yields

$$m_{\mathrm{W}}(ffff) \;=\; 80.242 \pm 0.048 \pm 0.031 \text{ GeV} . \tag{11}$$

In this combination the value of χ^2/d.o.f. is 29.2/27 and the weight of the fully-hadronic channel is 46%. In absence of any systematic uncertainties, the statistical precision of the measurement would be 47 MeV. In Table 4 the contributions of the individual sources of systematic uncertainty to this combined m_{W} result are given.

The results in this paper are combined with the direct measurements obtained at $\sqrt{s} = 172 - 184$ GeV [7] to give

$$m_{\mathrm{W}}(\mathrm{qq}\ell\nu) \;=\; 80.212 \pm 0.066 \pm 0.027 \text{ GeV} \quad \text{and} \tag{12}$$

$$m_{\mathrm{W}}(\mathrm{qqqq}) \;=\; 80.325 \pm 0.061 \pm 0.052 \text{ GeV} \quad , \tag{13}$$

with a correlation of 10%. Combining the results from direct measurements at $\sqrt{s} = 172 - 209$ GeV with those result obtained from cross section measurements at $\sqrt{s} = 161 - 172$ GeV [5] yields

$$m_{\mathrm{W}} \;=\; 80.270 \pm 0.046 \pm 0.031 \text{ GeV} . \tag{14}$$

The W-boson width is determined in fits for both m_{W} and Γ_{W}. Table 14 gives the results for $\sqrt{s} = 189 - 209$ GeV. Combining all data yields

$$\Gamma_{\mathrm{W}} \;=\; 2.18 \pm 0.11 \pm 0.09 \text{ GeV} . \tag{15}$$

References

[1] UA1 Collaboration, C. Albajar *et al.*, Z. Phys. **C 44** (1989) 15;
UA1 Collaboration, C. Albajar *et al.*, Phys. Lett. **B 253** (1991) 503;
UA2 Collaboration, J. Alitti *et al.*, Phys. Lett. **B 276** (1992) 354;
UA2 Collaboration, J. Alitti *et al.*, Phys. Lett. **B 276** (1992) 365.

[2] S.L. Glashow, Nucl. Phys. **22** (1961) 579;
S. Weinberg, Phys. Rev. Lett. **19** (1967) 1264;
A. Salam, in *Elementary Particle Theory*, ed. N. Svartholm (1968), 367;
G. 't Hooft and M. Veltman, Nucl. Phys. **B 44** (1972) 189.

[3] DØ Collaboration, B. Abbott *et al.*, Phys. Rev. **D 60** (1999) 052001;
CDF Collaboration, F. Abe *et al.*, Phys. Rev. **D 63** (2001) 032003;
DØ Collaboration, B. Abbott *et al.*, Nature **429** (2004) 638;
P. Azzi *et al.*, Preprint hep-ex/0404010 (2004).

[4] The ALEPH, DELPHI, L3, OPAL, SLD Collaborations, the LEP Electroweak Working Group, the SLD Electroweak and Heavy Flavour Groups, Preprint hep-ex/0509008 (2005).

[5] L3 Collaboration, M. Acciarri *et al.*, Phys. Lett. **B 407** (1997) 419;
L3 Collaboration, M. Acciarri *et al.*, Phys. Lett. **B 398** (1997) 223.

[6] ALEPH Collaboration, R. Barate *et al.*, Phys. Lett. **B 415** (1997) 435;
DELPHI Collaboration, P. Abreu *et al.*, Eur. Phys. J. **C 2** (1998) 581;
OPAL Collaboration, K. Ackerstaff *et al.*, Eur. Phys. J. **C 1** (1998) 395.

[7] L3 Collaboration, M. Acciarri *et al.*, Phys. Lett. **B 454** (1999) 386.

[8] ALEPH Collaboration, R. Barate *et al.*, Eur. Phys. J. **C 17** (2000) 241;
DELPHI Collaboration, P. Abreu *et al.*, Phys. Lett. **B 511** (2001) 159;
OPAL Collaboration, G. Abbiendi *et al.*, Preprint hep-ex/0508060 (2005).

[9] L3 Collaboration, B. Adeva *et al.*, Nucl. Inst. Meth. **A 289** (1990) 35;
L3 Collaboration, O. Adriani *et al.*, Phys. Rep. **236** (1993) 1;
M. Chemarin *et al.*, Nucl. Inst. Meth. **A 349** (1994) 345;
M. Acciarri *et al.*, Nucl. Inst. Meth. **A 351** (1994) 300;
G. Basti *et al.*, Nucl. Inst. Meth. **A 374** (1996) 293;
I.C. Brock *et al.*, Nucl. Inst. Meth. **A 381** (1996) 236;
A. Adam *et al.*, Nucl. Inst. Meth. **A 383** (1996) 342.

[10] CDF Collaboration, T. Affolder *et al.*, Phys. Rev. **D 64** (2001) 052001;
DØ Collaboration, B. Abbott *et al.*, Phys. Rev. **D 62** (2000) 092006;
CDF and DØ Collaborations, V.M. Abazov *et al.*, Phys. Rev. **D 70** (2004) 092008.

[11] S. Catani *et al.*, Phys. Lett. **B 269** (1991) 432;
S. Bethke *et al.*, Nucl. Phys. **B 370** (1992) 310.

[12] L3 Collaboration, P. Achard *et al.*, Phys. Lett. **B 600** (2004) 22.

[13] KANDY uses KORALW version 1.51 and YFSWW3 version 1.16.
S. Jadach *et al.*, Comp. Phys. Comm. **140** (2001) 475.

[14] RACOONWW version 1.3.1 is used.
A. Denner *et al.*, Comp. Phys. Comm. **153** (2003) 462.

[15] KK2F versions 4.14 and 4.19 are used.
S. Jadach *et al.*, Comp. Phys. Comm. **130** (2000) 260.

[16] PYTHIA version 6.2 is used.
T. Sjöstrand, Comp. Phys. Comm. **135** (2001) 238.

[17] HERWIG version 6.202 is used.
G. Marchesini *et al.*, Comp. Phys. Comm. **67** (1992) 465.

[18] ARIADNE version 4.12 is used.
L. Lönnblad, Comp. Phys. Comm. **71** (1992) 15.

[19] L3 Collaboration, P. Achard *et al.*, Phys. Rep. **399** (2004) 71.

[20] L. Lönnblad and T. Sjöstrand, Phys. Lett. **B 351** (1995) 293;
S. Jadach and K. Zalewski, Acta Phys. Pol. **B 28** (1997) 1363;
V. Kartvelishvili, R. Kvatadze and R. Møller, Phys. Lett. **B 408** (1997) 331;
K. Fialkowski and R. Wit, Z. Phys. **C 74** (1997) 145;
K. Fialkowski, R. Wit and J. Wosiek, Phys. Rev. **D 58** (1998) 094013.

[21] L. Lönnblad and T. Sjöstrand, Eur. Phys. J. **C 2** (1998) 165.

[22] L3 Collaboration, P. Achard *et al.*, Phys. Lett. **B 547** (2002) 139.

[23] G. Gustafson, U. Petterson and P.M. Zerwas, Phys. Lett. **B 209** (1988) 90;
T. Sjöstrand and V.A. Khoze, Z. Phys. **C 62** (1994) 281;
E. Accomando, A. Ballestrero and E. Maina, Phys. Lett. **B 362** (1995) 141;
G. Gustafson and J. Häkkinen, Z. Phys. **C 64** (1994) 659;
J. Ellis and K. Geiger, Phys. Rev. **D 54** (1996) 1967.

[24] L3 Collaboration, P. Achard *et al.*, Phys. Lett. **B 561** (2003) 202.

[25] GEANT version 3.15 is used.
R. Brun *et al.*, Report CERN-DD/EE/84-1 (1984), revised 1987.

[26] H. Fesefeldt, RWTH Aachen Preprint PITHA 85/02 (1985).

[27] R. Assmann *et al.*, Eur. Phys. J. **C 39** (2005) 253.

[28] W. Beenakker *et al.*, in *Physics at LEP 2*, Report CERN 96-01, Vol. 1, p. 79.

[29] EXCALIBUR version 1.113 is used.
F.A. Berends, R. Kleiss and R. Pittau, Comp. Phys. Comm. **85** (1995) 437.

[30] D.M. Schmidt, R.J. Morrison and M.S. Witherell, Nucl. Inst. Meth. **A 328** (1993) 547.

[31] L3 Collaboration, P. Achard *et al.*, Phys. Lett. **B 585** (2004) 42.

[32] L3 Collaboration, M. Acciarri *et al.*, Eur. Phys. J. **C 16** (2000) 1.

[33] R.G. Stuart, Phys. Lett. **B 262** (1991) 113;
A. Aeppli, F. Cuypers and G.J. van Oldenborgh, Phys. Lett. **B 314** (1993) 413;
H. Veltman, Z. Phys. **C 62** (1994) 35;
S. Jadach *et al.*, Phys. Lett. **B 417** (1998) 326;
A. Denner, S. Dittmaier and M. Roth, Nucl. Phys. **B 519** (1998) 39.

[34] D.R. Yennie, S.C. Frautschi and H. Suura, Ann. Phys. **13** (1961) 379.

[35] PHOTOS version 2.3 is used.
E. Barberio and Z. Wąs, Comp. Phys. Comm. **79** (1994) 291.

[36] D.Y. Bardin *et al.*, Phys. Lett. **B 206** (1988) 539;
Z. Kunszt *et al.*, in *Physics at LEP 2*, Report CERN 96-01, Vol. 1, p. 141.

[37] S. Jadach *et al.*, Phys. Lett. **B 523** (2001) 117.

[38] DELPHI Collaboration, P. Abreu *et al.*, Eur. Phys. J. **C 18** (2000) 203.

[39] L3 Collaboration, M. Acciarri *et al.*, Phys. Lett. **B 458** (1999) 517.

[40] L3 Collaboration, P. Achard *et al.*, Phys. Lett. **B 524** (2002) 55.

[41] V. Khoze and T. Sjöstrand, Eur. Phys. J. **C 6** (1999) 271.

[42] L. Lönnblad, Z. Phys. **C 70** (1996) 107.

[43] G. Corcella *et al.*, JHEP **01** (2001) 010.

[44] L3 Collaboration, P. Achard *et al.*, Phys. Lett. **B 581** (2004) 19.

[45] L. Lyons, D. Gibaut and P. Clifford, Nucl. Inst. Meth. **A 270** (1988) 110;
A. Valassi, Nucl. Inst. Meth. **A 500** (2003) 391.

The L3 Collaboration:

P.Achard,[20] O.Adriani,[17] M.Aguilar-Benitez,[25] J.Alcaraz,[25] G.Alemanni,[23] J.Allaby,[18] A.Aloisio,[29] M.G.Alviggi,[29] H.Anderhub,[49] V.P.Andreev,[6,34] F.Anselmo,[8] A.Arefiev,[28] T.Azemoon,[3] T.Aziz,[9] P.Bagnaia,[39] A.Bajo,[25] G.Baksay,[26] L.Baksay,[26] S.V.Baldew,[2] S.Banerjee,[9] Sw.Banerjee,[4] A.Barczyk,[49,47] R.Barillère,[18] P.Bartalini,[23] M.Basile,[8] N.Batalova,[46] R.Battiston,[33] A.Bay,[23] F.Becattini,[17] U.Becker,[13] F.Behner,[49] L.Bellucci,[17] R.Berbeco,[3] J.Berdugo,[25] P.Berges,[13] B.Bertucci,[33] B.L.Betev,[49] M.Biasini,[33] M.Biglietti,[29] A.Biland,[49] J.J.Blaising,[4] S.C.Blyth,[35] G.J.Bobbink,[2] A.Böhm,[1] L.Boldizsar,[12] B.Borgia,[39] S.Bottai,[17] D.Bourilkov,[49] M.Bourquin,[20] S.Braccini,[20] J.G.Branson,[41] F.Brochu,[4] J.D.Burger,[13] W.J.Burger,[33] A.Button,[3] X.D.Cai,[13] M.Capell,[13] G.Cara Romeo,[8] G.Carlino,[29] A.Cartacci,[17] J.Casaus,[25] F.Cavallari,[39] N.Cavallo,[36] C.Cecchi,[33] M.Cerrada,[25] M.Chamizo,[20] Y.H.Chang,[44] M.Chemarin,[24] A.Chen,[44] G.Chen,[7] G.M.Chen,[7] H.F.Chen,[22] H.S.Chen,[7] G.Chiefari,[29] L.Cifarelli,[40] F.Cindolo,[8] I.Clare,[13] R.Clare,[38] G.Coignet,[4] N.Colino,[25] S.Costantini,[39] B.de la Cruz,[25] S.Cucciarelli,[33] J.A.van Dalen,[31] R.de Asmundis,[29] P.Déglon,[20] J.Debreczeni,[12] A.Degré,[4] K.Dehmelt,[26] K.Deiters,[47] D.della Volpe,[29] E.Delmeire,[20] P.Denes,[37] F.DeNotaristefani,[39] A.De Salvo,[49] M.Diemoz,[39] M.Dierckxsens,[2] D.van Dierendonck,[2] C.Dionisi,[39] M.Dittmar,[49] A.Doria,[29] M.T.Dova,[10,♯] D.Duchesneau,[4] M.Duda,[1] B.Echenard,[20] A.Eline,[18] A.El Hage,[1] H.El Mamouni,[24] A.Engler,[35] F.J.Eppling,[13] P.Extermann,[20] M.A.Falagan,[25] S.Falciano,[39] A.Favara,[32] J.Fay,[24] O.Fedin,[34] M.Felcini,[49] T.Ferguson,[35] H.Fesefeldt,[1] E.Fiandrini,[33] J.H.Field,[20] F.Filthaut,[31] P.H.Fisher,[13] W.Fisher,[37] G.Forconi,[13] K.Freudenreich,[49] C.Furetta,[27] Yu.Galaktionov,[28,13] S.N.Ganguli,[9] P.Garcia-Abia,[25] M.Gataullin,[32] S.Gentile,[39] S.Giagu,[39] Z.F.Gong,[22] G.Grenier,[24] O.Grimm,[49] M.W.Gruenewald,[16] M.Guida,[40] V.K.Gupta,[37] A.Gurtu,[9] L.J.Gutay,[46] D.Haas,[5] D.Hatzifotiadou,[8] T.Hebbeker,[1] A.Hervé,[18] J.Hirschfelder,[35] H.Hofer,[49] M.Hohlmann,[26] G.Holzner,[49] S.R.Hou,[44] B.N.Jin,[7] P.Jindal,[14] L.W.Jones,[3] P.de Jong,[2] I.Josa-Mutuberría,[25] M.Kaur,[14] M.N.Kienzle-Focacci,[20] J.K.Kim,[43] J.Kirkby,[18] W.Kittel,[31] A.Klimentov,[13,28] A.C.König,[31] M.Kopal,[46] V.Koutsenko,[13,28] M.Kräber,[49] R.W.Kraemer,[35] A.Krüger,[48] A.Kunin,[13] P.Ladron de Guevara,[25] I.Laktineh,[24] G.Landi,[17] M.Lebeau,[18] A.Lebedev,[13] P.Lebrun,[24] P.Lecomte,[49] P.Lecoq,[18] P.Le Coultre,[49] J.M.Le Goff,[18] R.Leiste,[48] M.Levtchenko,[27] P.Levtchenko,[34] C.Li,[22] S.Likhoded,[48] C.H.Lin,[44] W.T.Lin,[44] F.L.Linde,[2] L.Lista,[29] Z.A.Liu,[7] W.Lohmann,[48] E.Longo,[39] Y.S.Lu,[7] C.Luci,[39] L.Luminari,[39] W.Lustermann,[49] W.G.Ma,[22] L.Malgeri,[18] A.Malinin,[28] C.Maña,[25] J.Mans,[37] J.P.Martin,[24] F.Marzano,[39] K.Mazumdar,[9] R.R.McNeil,[6] S.Mele,[18,29] L.Merola,[29] M.Meschini,[17] W.J.Metzger,[31] A.Mihul,[11] H.Milcent,[18] G.Mirabelli,[39] J.Mnich,[1] G.B.Mohanty,[9] T.Moulik,[9] G.S.Muanza,[24] A.J.M.Muijs,[2] M.Musy,[39] S.Nagy,[15] R.Nandakumar,[9] S.Natale,[20] M.Napolitano,[29] F.Nessi-Tedaldi,[49] H.Newman,[32] A.Nisati,[39] T.Novak,[31] H.Nowak,[48] R.Ofierzynski,[49] G.Organtini,[39] I.Pal,[46] C.Palomares,[25] P.Paolucci,[29] R.Paramatti,[39] G.Passaleva,[17] S.Patricelli,[29] T.Paul,[10] M.Pauluzzi,[33] C.Paus,[13] F.Pauss,[49] M.Pedace,[39] S.Pensotti,[27] D.Perret-Gallix,[4] D.Piccolo,[29] F.Pierella,[8] M.Pieri,[41] M.Pioppi,[33] P.A.Piroué,[37] E.Pistolesi,[27] V.Plyaskin,[28] M.Pohl,[20] V.Pojidaev,[17] J.Pothier,[18] D.Prokofiev,[34] G.Rahal-Callot,[49] M.A.Rahaman,[9] P.Raics,[15] N.Raja,[9] R.Ramelli,[49] P.G.Rancoita,[27] R.Ranieri,[17] A.Raspereza,[48] P.Razis,[30] S.Rembeczki,[26] D.Ren,[49] M.Rescigno,[39] S.Reucroft,[10] S.Riemann,[48] K.Riles,[3] B.P.Roe,[3] L.Romero,[25] A.Rosca,[48] C.Rosemann,[1] C.Rosenbleck,[1] S.Rosier-Lees,[4] S.Roth,[1] J.A.Rubio,[18] G.Ruggiero,[17] H.Rykaczewski,[49] A.Sakharov,[49] S.Saremi,[6] S.Sarkar,[39] J.Salicio,[18] E.Sanchez,[25] C.Schäfer,[18] V.Schegelsky,[34] H.Schopper,[21] D.J.Schotanus,[31] C.Sciacca,[29] L.Servoli,[33] S.Shevchenko,[32] N.Shivarov,[42] V.Shoutko,[13] E.Shumilov,[28] A.Shvorob,[32] D.Son,[43] C.Souga,[24] P.Spillantini,[17] M.Steuer,[13] D.P.Stickland,[37] B.Stoyanov,[42] A.Straessner,[20] K.Sudhakar,[9] G.Sultanov,[42] L.Z.Sun,[22] S.Sushkov,[1] H.Suter,[49] J.D.Swain,[10] W.Swomi,[18] Z.Szillasi,[26,¶] X.W.Tang,[7] P.Tarjan,[15] L.Tauscher,[5] L.Taylor,[10] B.Tellili,[24] D.Teyssier,[24] C.Timmermans,[31] Samuel C.C.Ting,[13] S.M.Ting,[13] S.C.Tonwar,[9] J.Tóth,[12] C.Tully,[37] K.L.Tung,[7] J.Ulbricht,[49] E.Valente,[39] R.T.Van de Walle,[31] R.Vasquez,[46] G.Vesztergombi,[12] I.Vetlitsky,[28] G.Viertel,[49] S.Villa,[38] M.Vivargent,[4] S.Vlachos,[5] I.Vodopianov,[26] H.Vogel,[35] H.Vogt,[48] I.Vorobiev,[35,28] A.A.Vorobyov,[34] M.Wadhwa,[5] Q.Wang,[31] X.L.Wang,[22] Z.M.Wang,[22] A.Weber,[1] M.Weber,[18] S.Wynhoff,[37] L.Xia,[32] Z.Z.Xu,[22] J.Yamamoto,[3] B.Z.Yang,[22] C.G.Yang,[7] H.J.Yang,[3] M.Yang,[7] S.C.Yeh,[45] An.Zalite,[34] Yu.Zalite,[34] Z.P.Zhang,[22] J.Zhao,[22] G.Y.Zhu,[7] R.Y.Zhu,[32] H.L.Zhuang,[7] A.Zichichi,[8,18,19] B.Zimmermann,[49] M.Zöller.[1]

1 III. Physikalisches Institut, RWTH, D-52056 Aachen, Germany[§]
2 National Institute for High Energy Physics, NIKHEF, and University of Amsterdam, NL-1009 DB Amsterdam, The Netherlands
3 University of Michigan, Ann Arbor, MI 48109, USA
4 Laboratoire d'Annecy-le-Vieux de Physique des Particules, LAPP,IN2P3-CNRS, BP 110, F-74941 Annecy-le-Vieux CEDEX, France
5 Institute of Physics, University of Basel, CH-4056 Basel, Switzerland
6 Louisiana State University, Baton Rouge, LA 70803, USA
7 Institute of High Energy Physics, IHEP, 100039 Beijing, China[△]
8 University of Bologna and INFN-Sezione di Bologna, I-40126 Bologna, Italy
9 Tata Institute of Fundamental Research, Mumbai (Bombay) 400 005, India
10 Northeastern University, Boston, MA 02115, USA
11 Institute of Atomic Physics and University of Bucharest, R-76900 Bucharest, Romania
12 Central Research Institute for Physics of the Hungarian Academy of Sciences, H-1525 Budapest 114, Hungary[‡]
13 Massachusetts Institute of Technology, Cambridge, MA 02139, USA
14 Panjab University, Chandigarh 160 014, India
15 KLTE-ATOMKI, H-4010 Debrecen, Hungary[¶]
16 UCD School of Physics, University College Dublin, Belfield, Dublin 4, Ireland
17 INFN Sezione di Firenze and University of Florence, I-50125 Florence, Italy
18 European Laboratory for Particle Physics, CERN, CH-1211 Geneva 23, Switzerland
19 World Laboratory, FBLJA Project, CH-1211 Geneva 23, Switzerland
20 University of Geneva, CH-1211 Geneva 4, Switzerland
21 University of Hamburg, D-22761 Hamburg, Germany
22 Chinese University of Science and Technology, USTC, Hefei, Anhui 230 029, China[△]
23 University of Lausanne, CH-1015 Lausanne, Switzerland
24 Institut de Physique Nucléaire de Lyon, IN2P3-CNRS,Université Claude Bernard, F-69622 Villeurbanne, France
25 Centro de Investigaciones Energéticas, Medioambientales y Tecnológicas, CIEMAT, E-28040 Madrid, Spain[♭]
26 Florida Institute of Technology, Melbourne, FL 32901, USA
27 INFN-Sezione di Milano, I-20133 Milan, Italy
28 Institute of Theoretical and Experimental Physics, ITEP, Moscow, Russia
29 INFN-Sezione di Napoli and University of Naples, I-80125 Naples, Italy
30 Department of Physics, University of Cyprus, Nicosia, Cyprus
31 Radboud University and NIKHEF, NL-6525 ED Nijmegen, The Netherlands
32 California Institute of Technology, Pasadena, CA 91125, USA
33 INFN-Sezione di Perugia and Università Degli Studi di Perugia, I-06100 Perugia, Italy
34 Nuclear Physics Institute, St. Petersburg, Russia
35 Carnegie Mellon University, Pittsburgh, PA 15213, USA
36 INFN-Sezione di Napoli and University of Potenza, I-85100 Potenza, Italy
37 Princeton University, Princeton, NJ 08544, USA
38 University of Californa, Riverside, CA 92521, USA
39 INFN-Sezione di Roma and University of Rome, "La Sapienza", I-00185 Rome, Italy
40 University and INFN, Salerno, I-84100 Salerno, Italy
41 University of California, San Diego, CA 92093, USA
42 Bulgarian Academy of Sciences, Central Lab. of Mechatronics and Instrumentation, BU-1113 Sofia, Bulgaria
43 The Center for High Energy Physics, Kyungpook National University, 702-701 Taegu, Republic of Korea
44 National Central University, Chung-Li, Taiwan, China
45 Department of Physics, National Tsing Hua University, Taiwan, China
46 Purdue University, West Lafayette, IN 47907, USA
47 Paul Scherrer Institut, PSI, CH-5232 Villigen, Switzerland
48 DESY, D-15738 Zeuthen, Germany
49 Eidgenössische Technische Hochschule, ETH Zürich, CH-8093 Zürich, Switzerland
§ Supported by the German Bundesministerium für Bildung, Wissenschaft, Forschung und Technologie.
‡ Supported by the Hungarian OTKA fund under contract numbers T019181, F023259 and T037350.
¶ Also supported by the Hungarian OTKA fund under contract number T026178.
♭ Supported also by the Comisión Interministerial de Ciencia y Tecnología.
♯ Also supported by CONICET and Universidad Nacional de La Plata, CC 67, 1900 La Plata, Argentina.
△ Supported by the National Natural Science Foundation of China.

		qqeν		qq$\mu\nu$		qq$\tau\nu$		qqqq	
$\langle\sqrt{s}\rangle$ [GeV]	$\mathcal{L}$ [pb^{-1}]	$N_{\rm data}$	$N_{\rm back}$	$N_{\rm data}$	$N_{\rm back}$	$N_{\rm data}$	$N_{\rm back}$	$N_{\rm data}$	$N_{\rm back}$
188.6	176.8	347	22.9	341	14.9	413	69.7	1477	328.7
191.6	29.8	73	4.1	63	2.4	57	11.9	236	57.5
195.5	84.1	168	10.9	157	8.2	222	33.8	665	153.5
199.6	83.3	152	11.4	142	7.3	181	32.2	726	151.1
201.8	37.1	70	5.3	79	3.4	77	13.9	301	64.6
204.8	79.0	176	11.0	142	6.5	164	26.4	656	137.2
206.6	139.1	283	18.0	263	12.5	304	48.0	1173	234.2
Total	629.4	1269	83.6	1187	55.2	1418	235.9	5234	1126.8

Table 1: Integrated luminosity, $\mathcal{L}$, together with the number of selected data events, $N_{\rm data}$, and expected number of background events, $N_{\rm back}$, for each final state and average value of $\sqrt{s}$.

	Energy [%]	θ [deg.]	ϕ [deg.]
Electrons	1.4	0.47	0.083
Muons	5.2	0.22	0.007
Hadronic jets (no cut)	15	2.4	1.9
Hadronic jets ($E_C > 2$ GeV)	15	2.5	2.1

Table 2: Average energy and angle resolutions for reconstructed electrons, muons and hadronic jets as determined in Monte Carlo simulation. Resolutions for hadronic jets are given with and without the cut on the minimum cluster energy, E_C.

Mass variable	qqeν	qq$\mu\nu$	qq$\tau\nu$	qqqq 4-jet	qqqq 5-jet	used in fit as
$m_{\rm raw}^{\rm qq}$	8.4	8.5	10.8	11.6	12.4	
$m_{\rm raw}$	5.1	7.5	–	6.6	6.7	
$m_{\rm resc}$	–	–	4.4	–	–	m_1
$m_{\rm 1C}$	4.7	6.5	–	–	–	m_2
$m_{\rm 2C}$	2.3	2.8	–	–	–	m_1
$m_{\rm 4C}$	–	–	–	2.2	3.0	m_2
$m_{\rm 5C}$	–	–	–	1.9	2.5	m_1

Table 3: Mass resolutions in GeV as determined in Monte Carlo simulation: raw mass resolution, $m_{\rm raw}^{\rm qq}$, of the hadronically-decaying W bosons; resolution of the average of the two raw masses in each event, $m_{\rm raw}$; resolution after rescaling the jet energies, $m_{\rm resc}$, or after applying a kinematic fit, $m_{n\rm C}$. The last column indicates which of the mass variables is used for each final state in the extraction of $m_{\rm W}$ and $\Gamma_{\rm W}$, as described in Section 5.

	qqeν	qq$\mu\nu$	qq$\tau\nu$	qqqq	qq$\ell\nu$	$ffff$
Calibration of $\sqrt{s}$	10				10	10
Lepton measurement	6	12	–	–	5	3
Jet measurement	4	11	23	5	9	7
Background	2	1	23	7	3	4
MC statistics	7	9	22	10	5	6
Photon radiation	16	10	9	6	13	10
Hadronisation	11	12	44	20	16	18
Bose-Einstein correlations	–	–	–	17	–	8
Colour reconnection	–	–	–	38	–	17
Total systematic	24	26	60	49	26	31
Total statistical	99	119	175	64	70	48
Total	102	121	185	81	74	57

Table 4: Systematic uncertainties on m_{W}, in MeV, for the various final states. The values refer to the complete data set at $\sqrt{s} = 189 - 209$ GeV and take into account correlations between energy points and final states.

	qqeν	qq$\mu\nu$	qq$\tau\nu$	qqqq	qq$\ell\nu$	$ffff$
Calibration of $\sqrt{s}$	<5				<5	<5
Lepton measurement	10	35	–	–	15	5
Jet measurement	20	30	75	20	30	25
Background	20	5	45	50	10	25
MC statistics	15	20	50	15	15	10
Photon radiation	5	5	5	5	5	5
Hadronisation	55	70	150	85	75	80
Bose-Einstein correlations	–	–	–	10	–	5
Colour reconnection	–	–	–	50	–	25
Total systematic	65	90	180	115	85	90
Total statistical	245	305	380	150	170	115
Total	255	315	420	190	190	145

Table 5: Systematic uncertainties on Γ_{W}, in MeV, for the various final states. All uncertainties are rounded to the next 5 MeV. The values refer to the complete data set at $\sqrt{s} = 189-209$ GeV and take into account correlations between energy points and final states.

	$\lvert\Delta m_{\mathrm{W}}\rvert$ [MeV]				$\lvert\Delta\Gamma_{\mathrm{W}}\rvert$ [MeV]			
	qqeν	qq$\mu\nu$	qq$\tau\nu$	qqqq	qqeν	qq$\mu\nu$	qq$\tau\nu$	qqqq
Electron energy	6	–	–	–	12	–	–	–
Muon energy	–	12	–	–	–	37	–	–
Jet energy scale ($\pm$50 MeV)	3	10	9	2	1	9	16	4
Jet energy smearing (1%)	1	4	7	1	10	25	53	7
Jet angle smearing (0.5°)	2	4	20	4	17	16	47	18

Table 6: Changes of m_{W} and Γ_{W} due to variations of the energy measurement of electrons, muons and jets and the resolutions of the jet directions.

	$\lvert\Delta m_{\mathrm{W}}\rvert$ [MeV]				$\lvert\Delta\Gamma_{\mathrm{W}}\rvert$ [MeV]			
	qqeν	qq$\mu\nu$	qq$\tau\nu$	qqqq	qqeν	qq$\mu\nu$	qq$\tau\nu$	qqqq
Four-fermion background	2	1	2	3	12	1	12	11
$\mathrm{e^+e^-} \to \mathrm{qq}$ background	<1	<1	23	3	15	6	44	31
y_{34} spectrum	–	–	–	5	–	–	–	40

Table 7: Changes of m_{W} and Γ_{W} due to variations of the background processes. For fully-hadronic events the uncertainty due to the y_{34} spectrum is also given.

	Δm_{W} [MeV]				$\Delta\Gamma_{\mathrm{W}}$ [MeV]			
	qqeν	qq$\mu\nu$	qq$\tau\nu$	qqqq	qqeν	qq$\mu\nu$	qq$\tau\nu$	qqqq
Generator comparison	-16	$+9$	–	$+4$	–	–	–	–
Monte Carlo reweighting	0	-5	-1	$+5$	$+3$	$+5$	-3	-3

Table 8: Changes of m_{W} and Γ_{W} due to variations in the modelling of photon radiation. The first row gives the results of a comparison between the RACOONWW and KANDY generators. The second row gives the difference between the $\mathcal{O}(\alpha^3)$ and the $\mathcal{O}(\alpha^2)$ calculation, obtained by reweighting KANDY events. The statistical accuracy of the generator comparison is about 8 MeV, while the statistical uncertainty of the reweighting procedure is negligible.

	Δm_{W} [MeV]				$\Delta\Gamma_{\mathrm{W}}$ [MeV]			
	qqeν	qq$\mu\nu$	qq$\tau\nu$	qqqq	qqeν	qq$\mu\nu$	qq$\tau\nu$	qqqq
HERWIG	0	-8	-41	-3	-96	-141	-275	-32
ARIADNE	-15	-11	-44	$+11$	$+15$	-1	-24	$+5$

Table 9: Changes of m_{W} and Γ_{W} due to the use of the hadronisation models HERWIG and ARIADNE instead of PYTHIA. The statistical accuracy is always better than 15 MeV and 30 MeV for m_{W} and Γ_{W}, respectively.

	Δm_{W} [MeV]		$\Delta\Gamma_{\mathrm{W}}$ [MeV]	
	qq$\ell\nu$	qqqq	qq$\ell\nu$	qqqq
Kaon multiplicity	$+13 \pm 12$	$+25 \pm 23$	-12 ± 11	-95 ± 87
Proton multiplicity	$+1 \pm 2$	$+7 \pm 15$	-3 ± 5	-36 ± 80

Table 10: Changes of m_{W} and Γ_{W} due to reweighting Monte Carlo events with respect to variations of the mean charged-kaon and proton multiplicities. The given uncertainties are due to the experimental uncertainties in the determination of these multiplicities [38].

$\sqrt{s}$ [GeV]	Δm_{W} [MeV]	$\Delta\Gamma_{\mathrm{W}}$ [MeV]
189	$+11$	-1
207	$+23$	-15

Table 11: Changes of m_{W} and Γ_{W} in the qqqq channel when replacing our standard simulation by the PYTHIA BE32 model with a strength of inter-W BEC corresponding to the 68% upper limit set by our direct BEC measurement [22]. The statistical accuracy is 6 MeV and 14 MeV for m_{W} and Γ_{W}, respectively.

$\sqrt{s}$ [GeV]	Δm_{W} [MeV]	$\Delta\Gamma_{\mathrm{W}}$ [MeV]
189	-22	-48
207	-57	-56

Table 12: Changes of m_{W} and Γ_{W} in the qqqq final state when replacing our standard simulation by the PYTHIA SK-I model with $k_{\mathrm{I}} = 1.1$ which is the 68% upper limit set by our CR measurement [24]. The cut on the minimum cluster energy of 2 GeV is applied. The statistical accuracies are about 10 MeV for m_{W} and 20 MeV for Γ_{W}.

Process	m_{W} [GeV]	$\sigma_{\mathrm{stat}}^{\mathrm{exp}}$ [GeV]
$\mathrm{e^+e^-} \to \mathrm{qqe}\nu$	$80.225 \pm 0.099 \pm 0.024$	0.095
$\mathrm{e^+e^-} \to \mathrm{qq}\mu\nu$	$80.152 \pm 0.119 \pm 0.026$	0.119
$\mathrm{e^+e^-} \to \mathrm{qq}\tau\nu$	$80.195 \pm 0.175 \pm 0.060$	0.162
$\mathrm{e^+e^-} \to \mathrm{qq}\ell\nu$	$80.196 \pm 0.070 \pm 0.026$	0.068
$\mathrm{e^+e^-} \to \mathrm{qqqq}$	$80.298 \pm 0.064 \pm 0.049$	0.062
$\mathrm{e^+e^-} \to ffff$	$80.242 \pm 0.048 \pm 0.031$	0.047

Table 13: Results on m_{W} for the data collected at $\sqrt{s} = 189-209$ GeV. The first uncertainty is statistical and the second systematic. Also shown is the expected statistical uncertainty, $\sigma_{\mathrm{stat}}^{\mathrm{exp}}$.

Process	m_{W} [GeV]	Γ_{W} [GeV]	Correlation
$\mathrm{e^+e^-} \to \mathrm{qq}\ell\nu$	$80.174 \pm 0.078 \pm 0.027$	$2.50 \pm 0.17 \pm 0.09$	0.01
$\mathrm{e^+e^-} \to \mathrm{qqqq}$	$80.284 \pm 0.074 \pm 0.050$	$1.97 \pm 0.15 \pm 0.12$	0.15
$\mathrm{e^+e^-} \to ffff$	$80.236 \pm 0.054 \pm 0.032$	$2.22 \pm 0.11 \pm 0.09$	0.14

Table 14: Results on m_{W} and Γ_{W} obtained from a simultaneous fit of both quantities using data collected at $\sqrt{s} = 189 - 209$ GeV. The first uncertainty is statistical and the second systematic. Also quoted is the correlation between m_{W} and Γ_{W}.

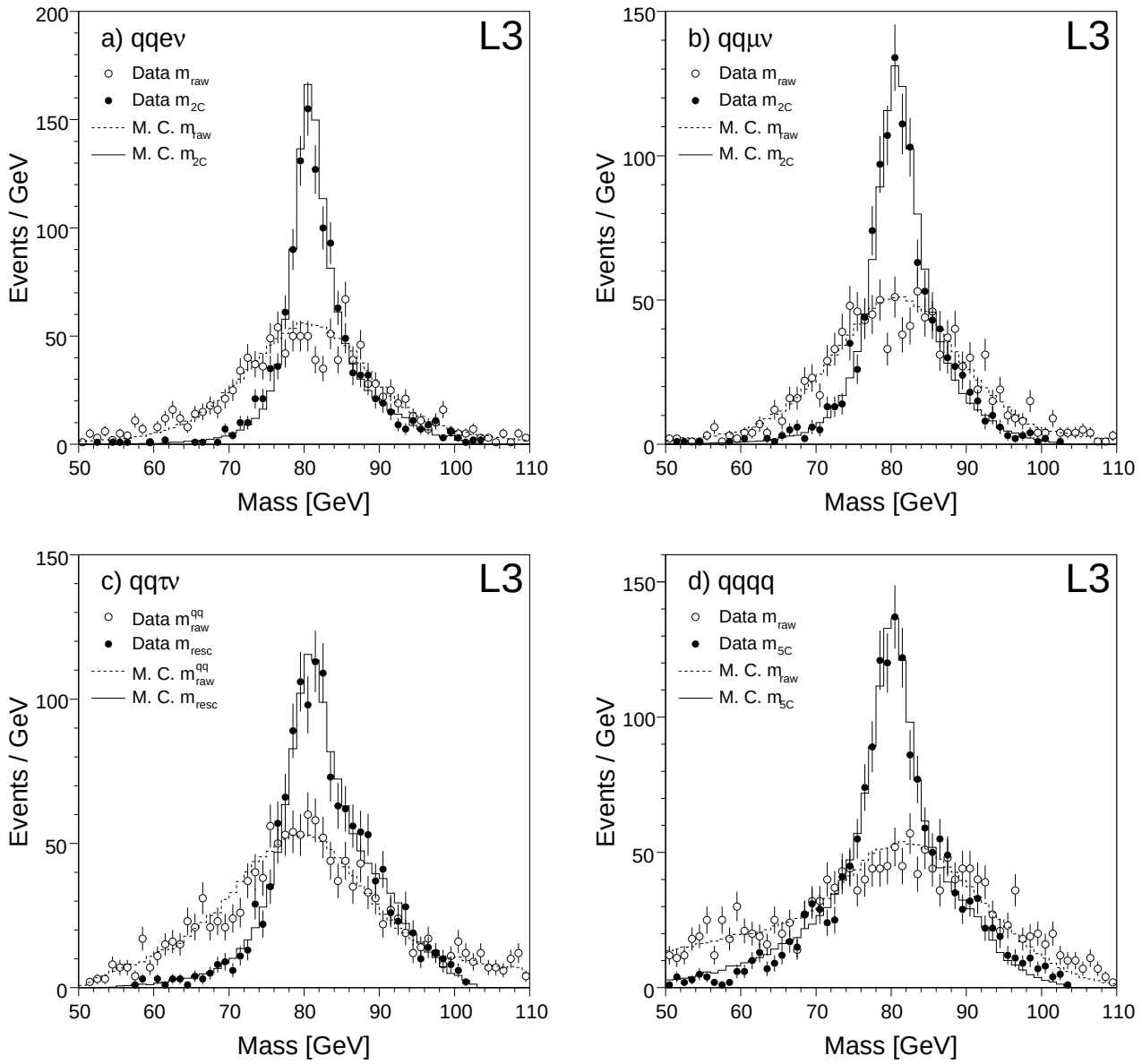

Figure 1: Improvement of mass resolutions due to kinematic constraints for a) qqeν, b) qq$\mu\nu$, c) qq$\tau\nu$ and d) qqqq events. The open circles represent the raw mass spectra and the full points the spectra obtained after applying the kinematic fit or the jet-energy rescaling. Monte Carlo predictions are also shown. In a), b) and d) $m_{\rm raw}$ is the average of the two raw masses while in c) $m_{\rm raw}^{\rm qq}$ is the raw mass of the hadronic system.

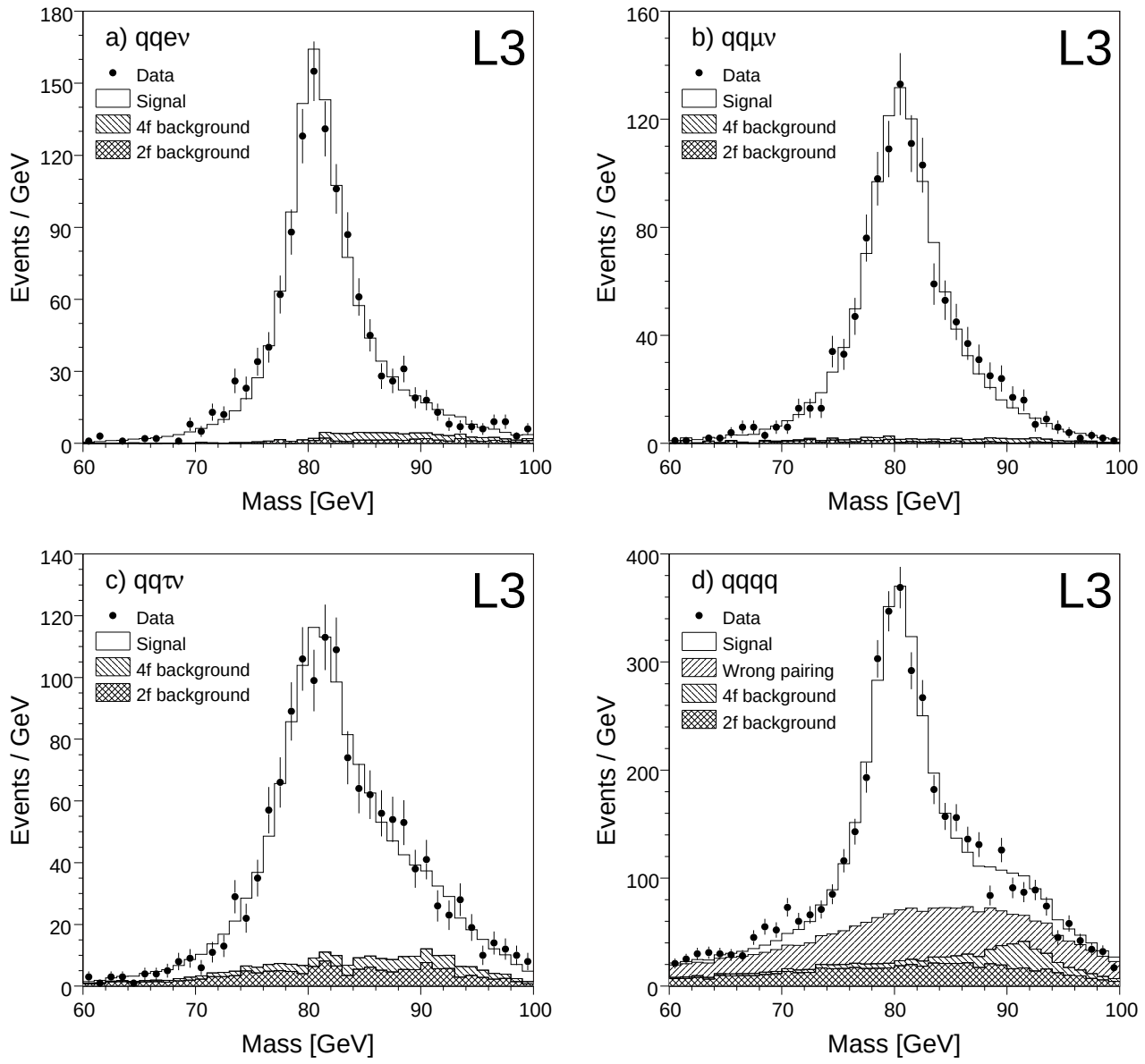

Figure 2: Distributions of reconstructed W-boson masses after applying the kinematic fit using the equal-mass constraint for the a) qqeν, b) qq$\mu\nu$ and c) qq$\tau\nu$ channels and d) the best pairing for the qqqq channel. The signal Monte Carlo events are reweighted according to the fitted value of m_{W}.

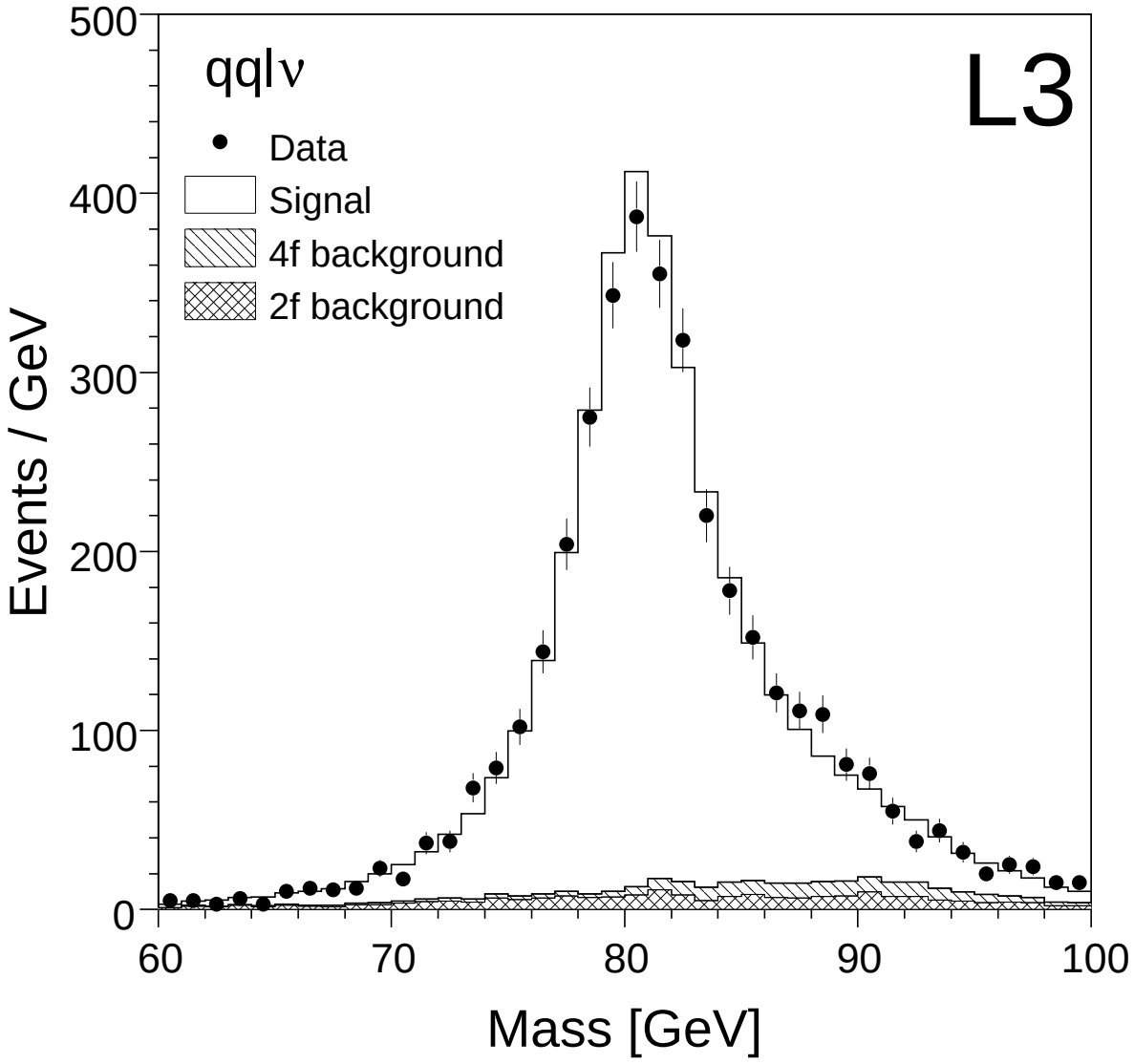

Figure 3: Distribution of reconstructed W-boson masses after applying the kinematic fit using the equal-mass constraint for semi-leptonic final states. The signal Monte Carlo events are reweighted according to the fitted value of m_{W}.

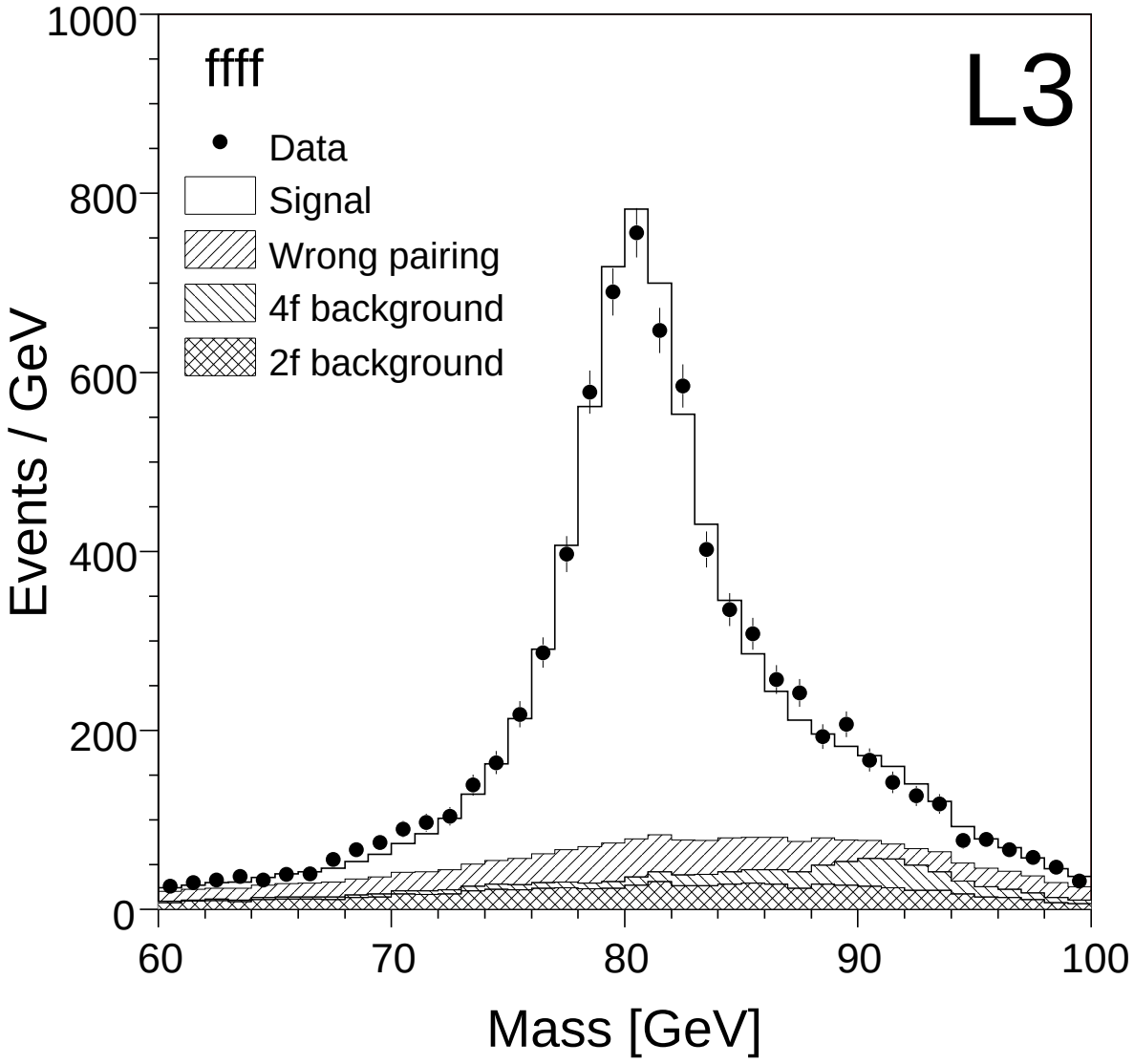

Figure 4: Distribution of reconstructed W-boson masses after applying the kinematic fit using the equal-mass constraint for all W pairs. The signal Monte Carlo events are reweighted according to the fitted value of m_{W}.

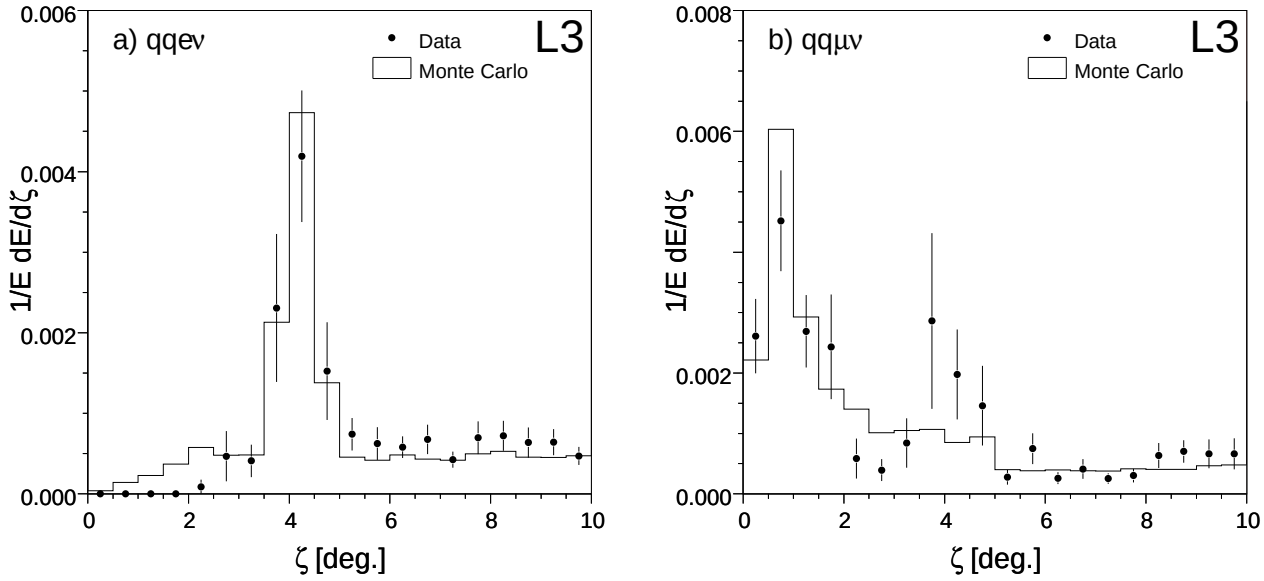

Figure 5: Calorimetric energy-flow versus the angle relative to the direction of the charged lepton, ζ, for a) the qqeν and b) the qq$\mu\nu$ events. The error bars represent the standard deviation of the data distribution in each bin.

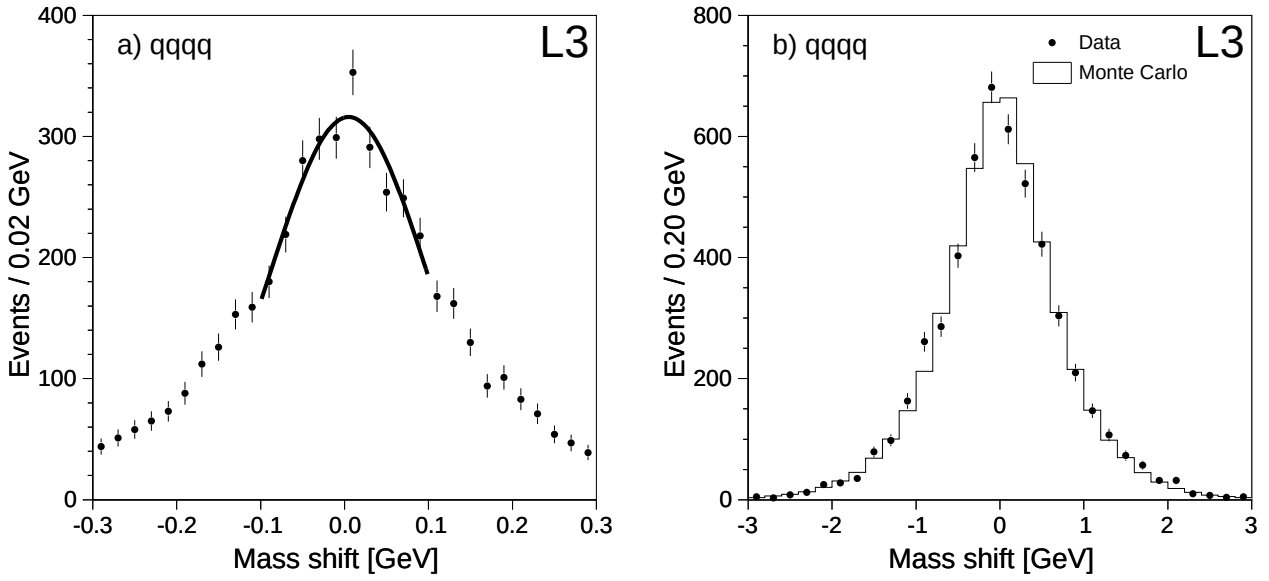

Figure 6: Distribution of the mass shifts between the standard analysis of qqqq events and analyses using a) a displaced vertex and b) jet reconstruction from tracking information only. A Gaussian fit is applied to the data distribution of a) and indicates an average mass shift consistent with zero, as shown by the curve. The data distribution of b) is in good agreement with the Monte Carlo prediction.

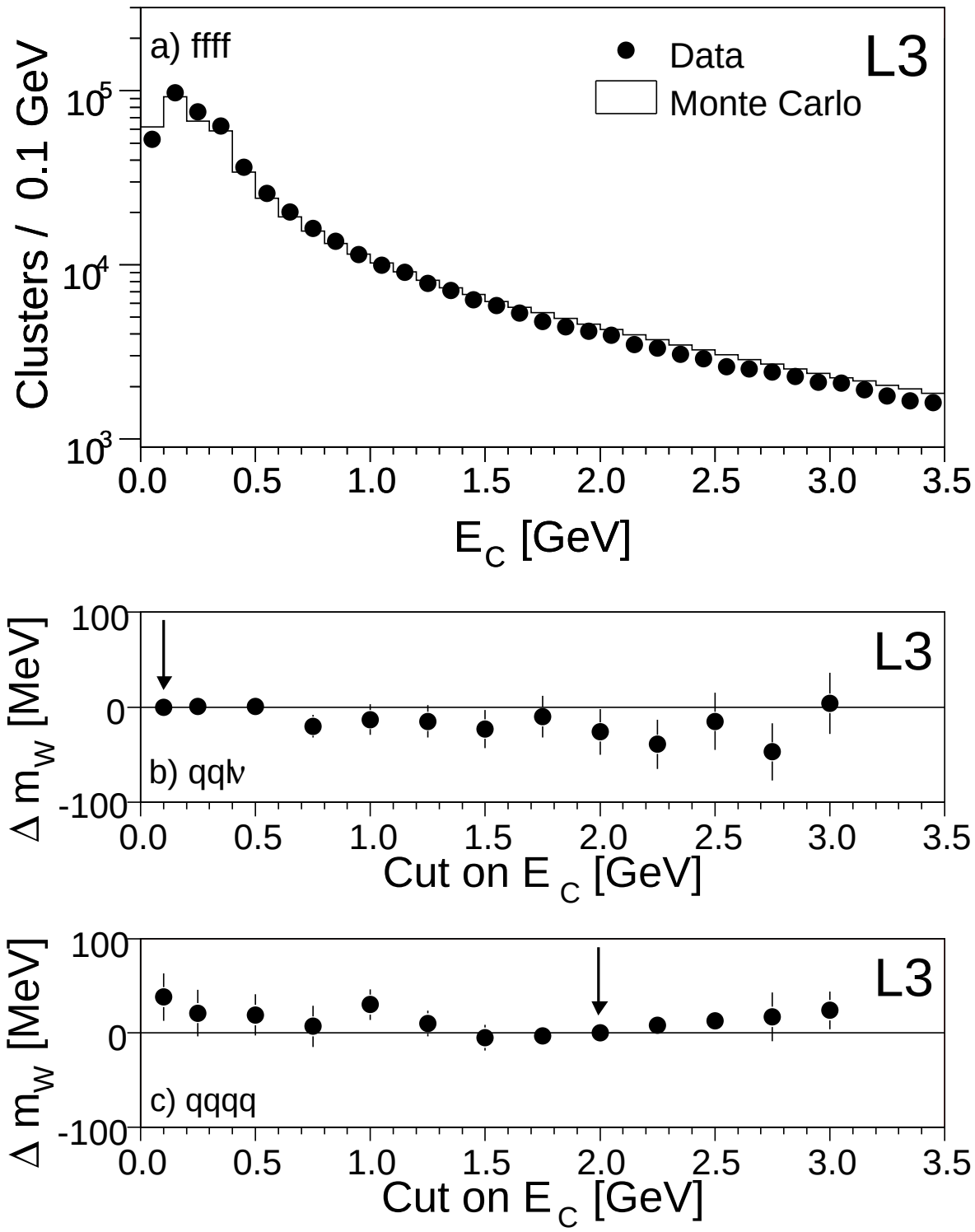

Figure 7: a) Energy spectrum of the clusters used in the jet reconstruction and changes of m_{W} for b) the qq$\ell\nu$ and c) the qqqq final states caused by a variation of the cut on the minimum cluster energy, E_C. The arrows show the default values of the cut.

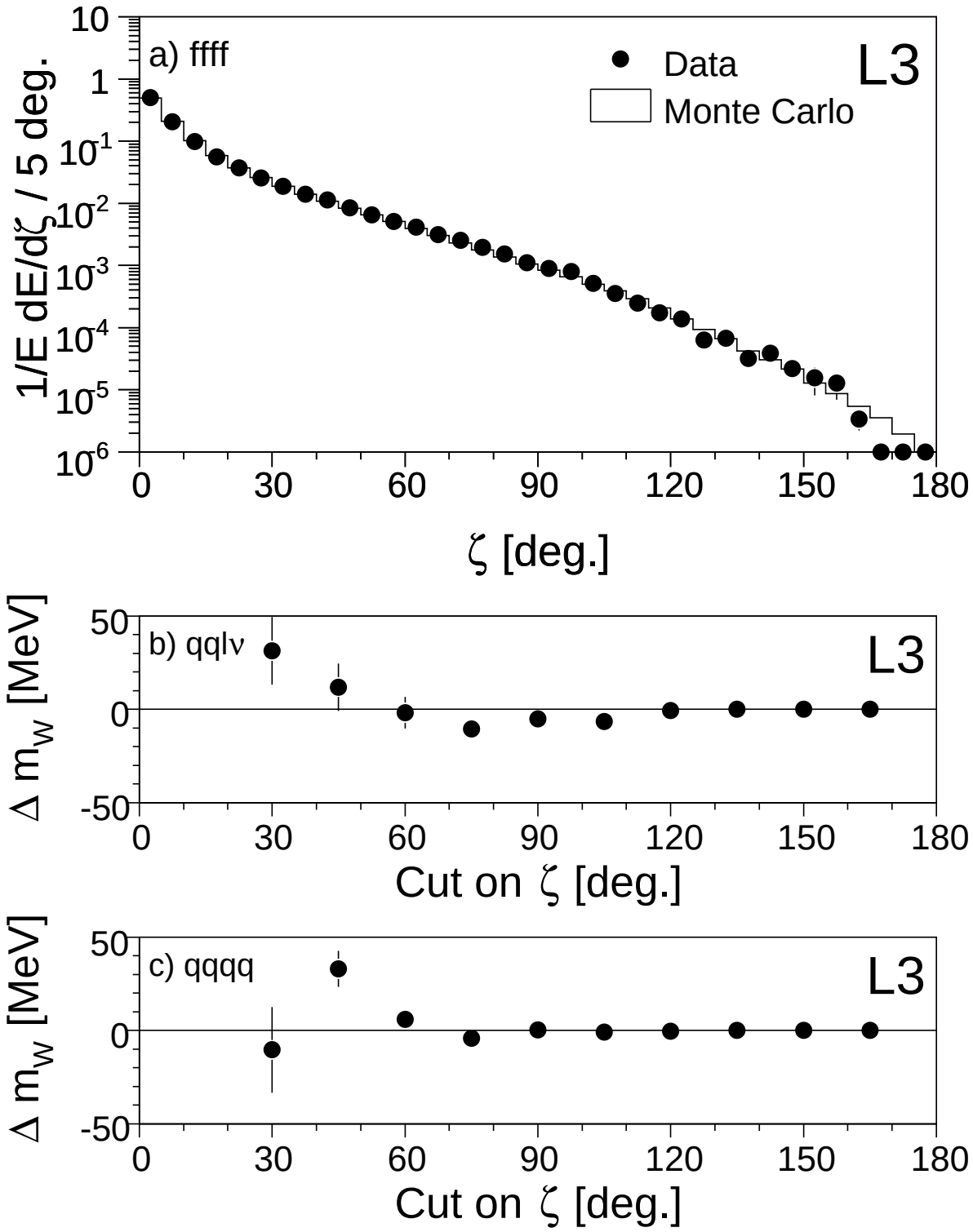

Figure 8: a) Energy flow as a function of the angle relative to the jet direction, ζ, and changes of m_{W} for b) the qq$\ell\nu$ and c) the qqqq final states after removing clusters outside a cone of half-opening angle ζ around the jet direction.

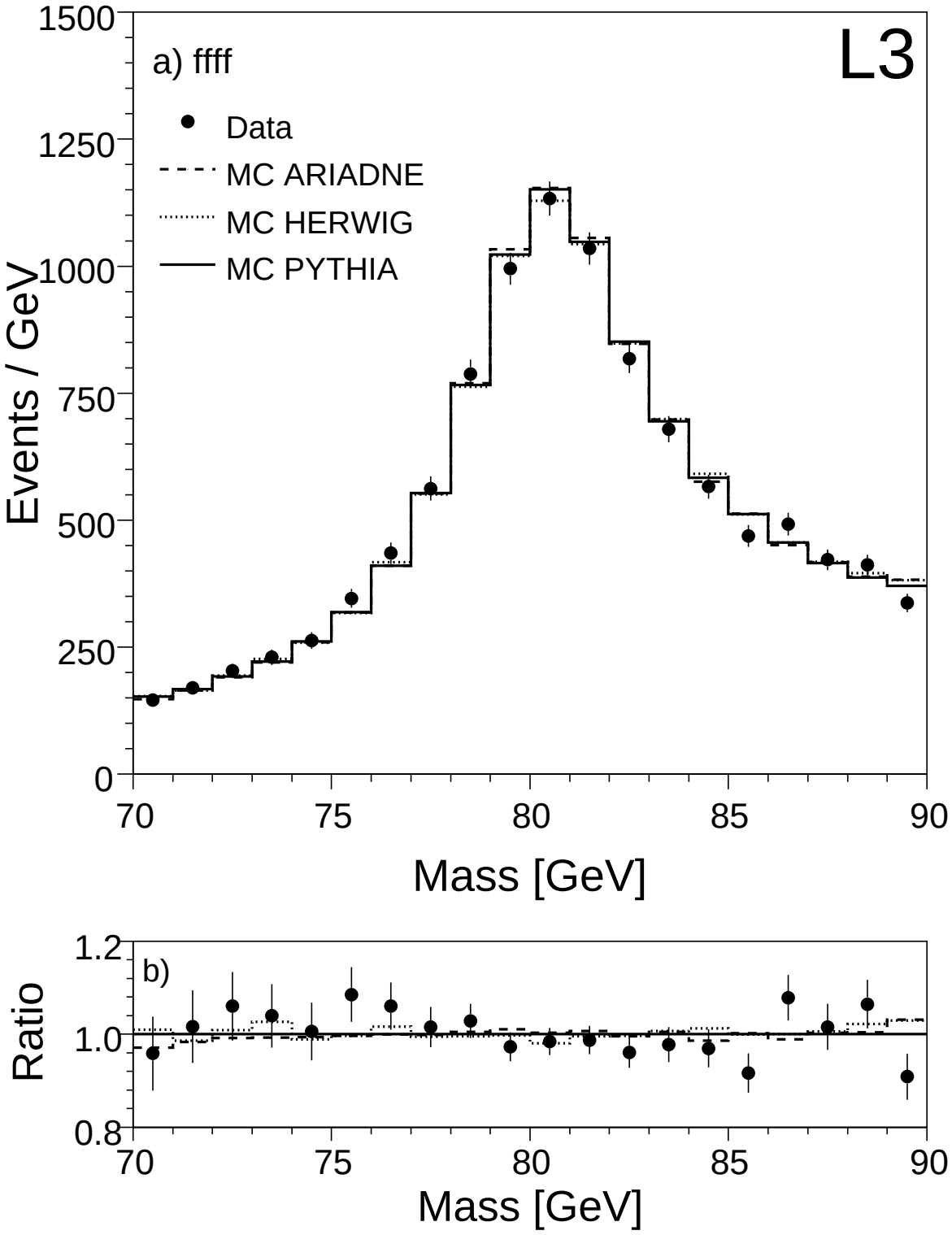

Figure 9: a) Comparison of the reconstructed mass spectra, combined for all final states at $\sqrt{s}$ = 189 GeV, for data and for the three hadronisation models PYTHIA, ARIADNE and HERWIG and b) the spectra normalised to the PYTHIA expectation.

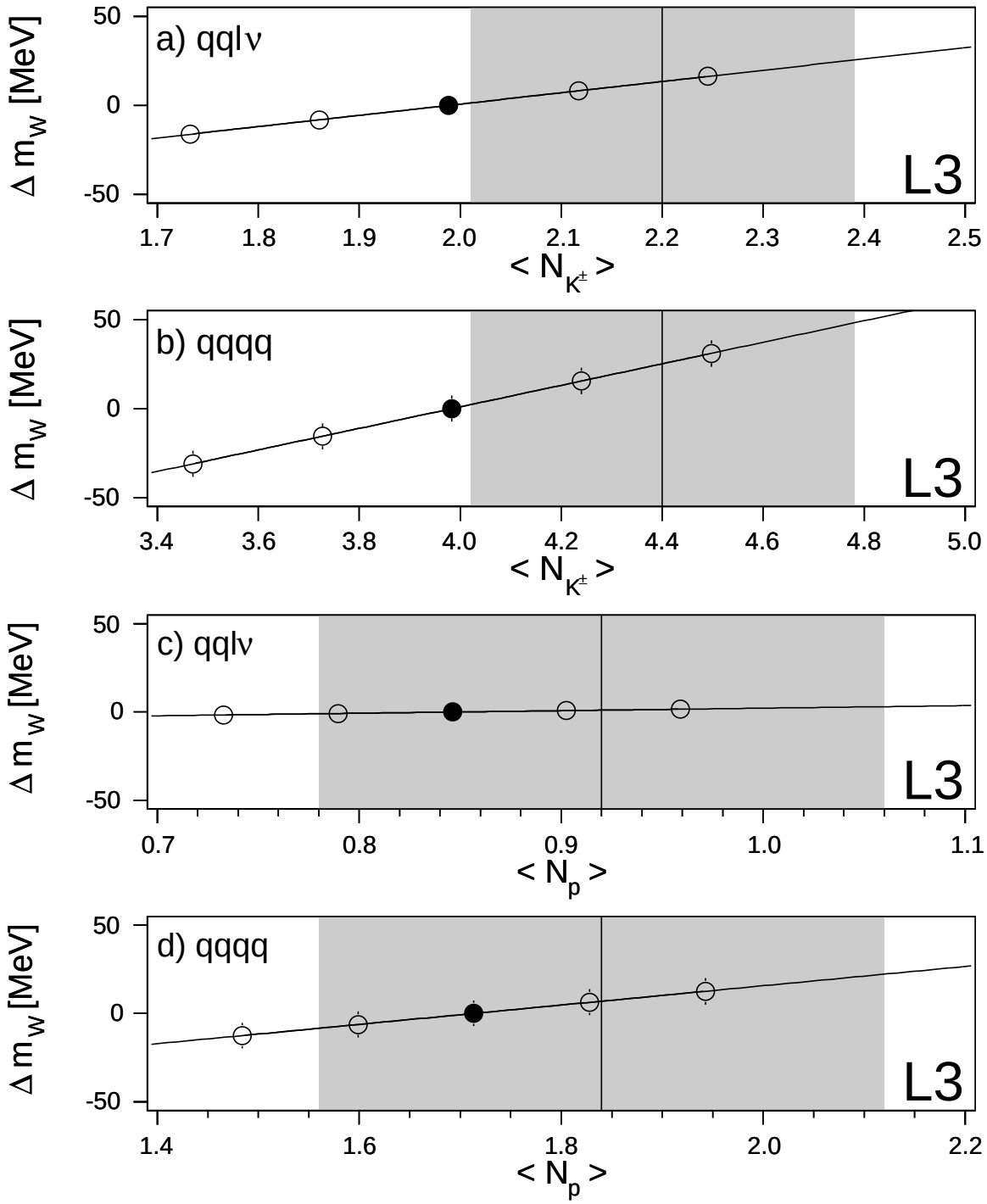

Figure 10: Changes of m_{W} due to reweighting Monte Carlo events according to the mean charged-kaon multiplicity for a) the qq$\ell\nu$ and b) the qqqq events and of the mean proton multiplicity for c) the qq$\ell\nu$ and d) the qqqq events. The full circles show the default values of our simulation whereas the vertical lines show the measured multiplicities and the grey bands their uncertainties [38].

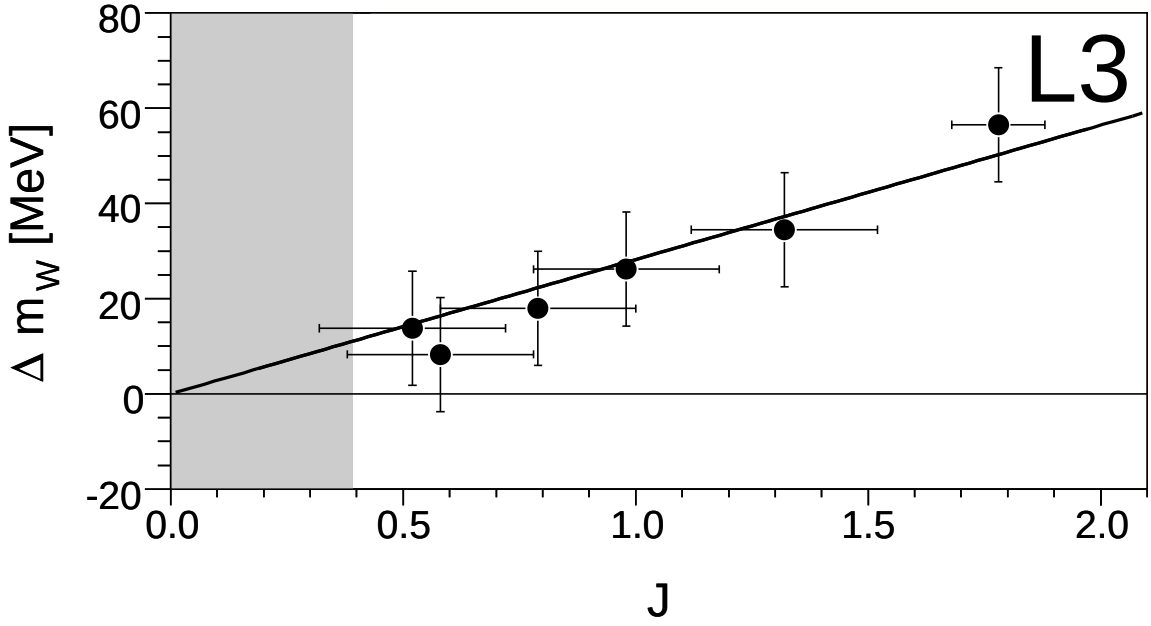

Figure 11: Changes of m_{W} with respect to the observable J for Monte Carlo samples of the BE32 model with different BEC parameters at $\sqrt{s} = 189$ GeV. The grey band shows the range of J which is compatible with our BEC measurement [22] at the 68% confidence level.

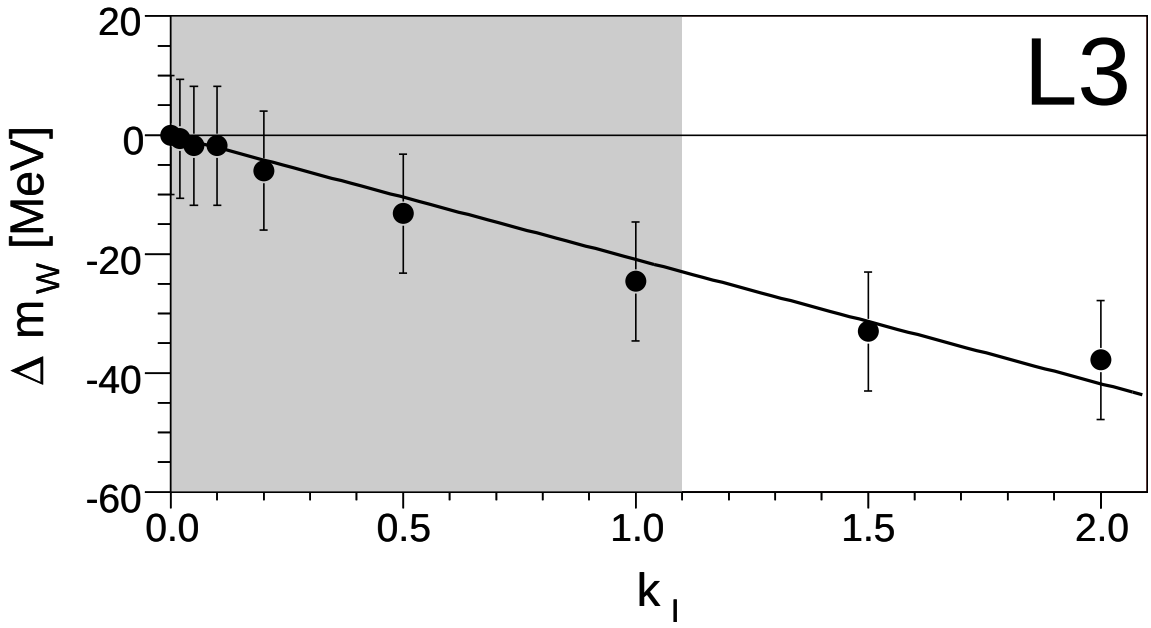

Figure 12: Changes of m_{W} with respect to the parameter k_{I} of the SK-I model at $\sqrt{s} = 189$ GeV. The cut on the minimum cluster energy of 2 GeV is applied. The grey band shows the range of k_{I} which is compatible with our CR measurement [24] at the 68% confidence level.

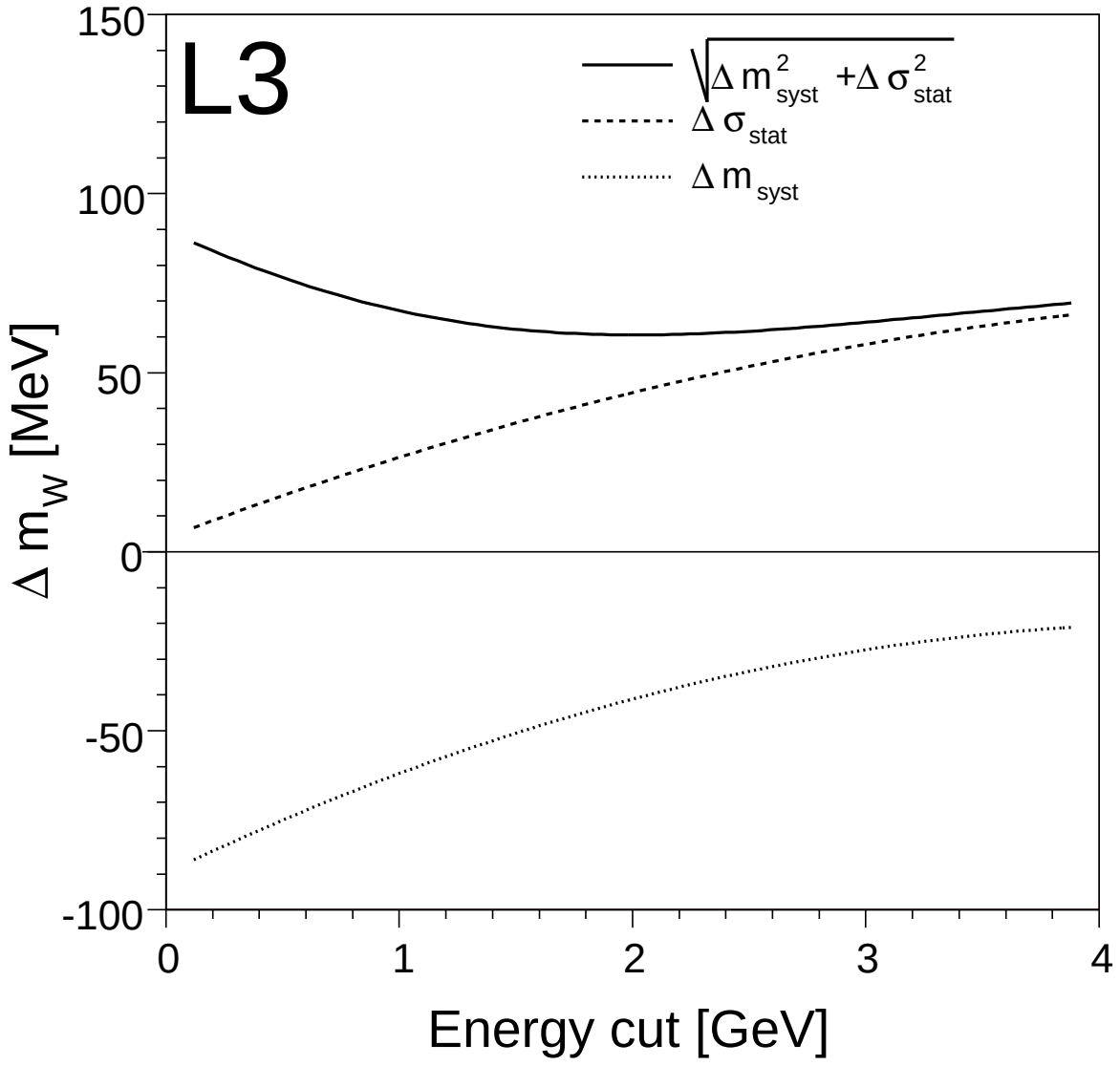

Figure 13: CR effects simulated with the Monte Carlo model SK-I calculated after removing clusters with an energy below a given threshold energy. The change of the final m_{W} measurement in the qqqq channel, Δm_{syst}, when the default simulation without CR is replaced by the SK-I model using $k_{\mathrm{I}} = 1.1$ is shown. The additional component of the statistical uncertainty on the final m_{W} result, $\Delta\sigma_{\mathrm{stat}}$, after applying the given energy cut and the quadratic sum of both effects is also shown.

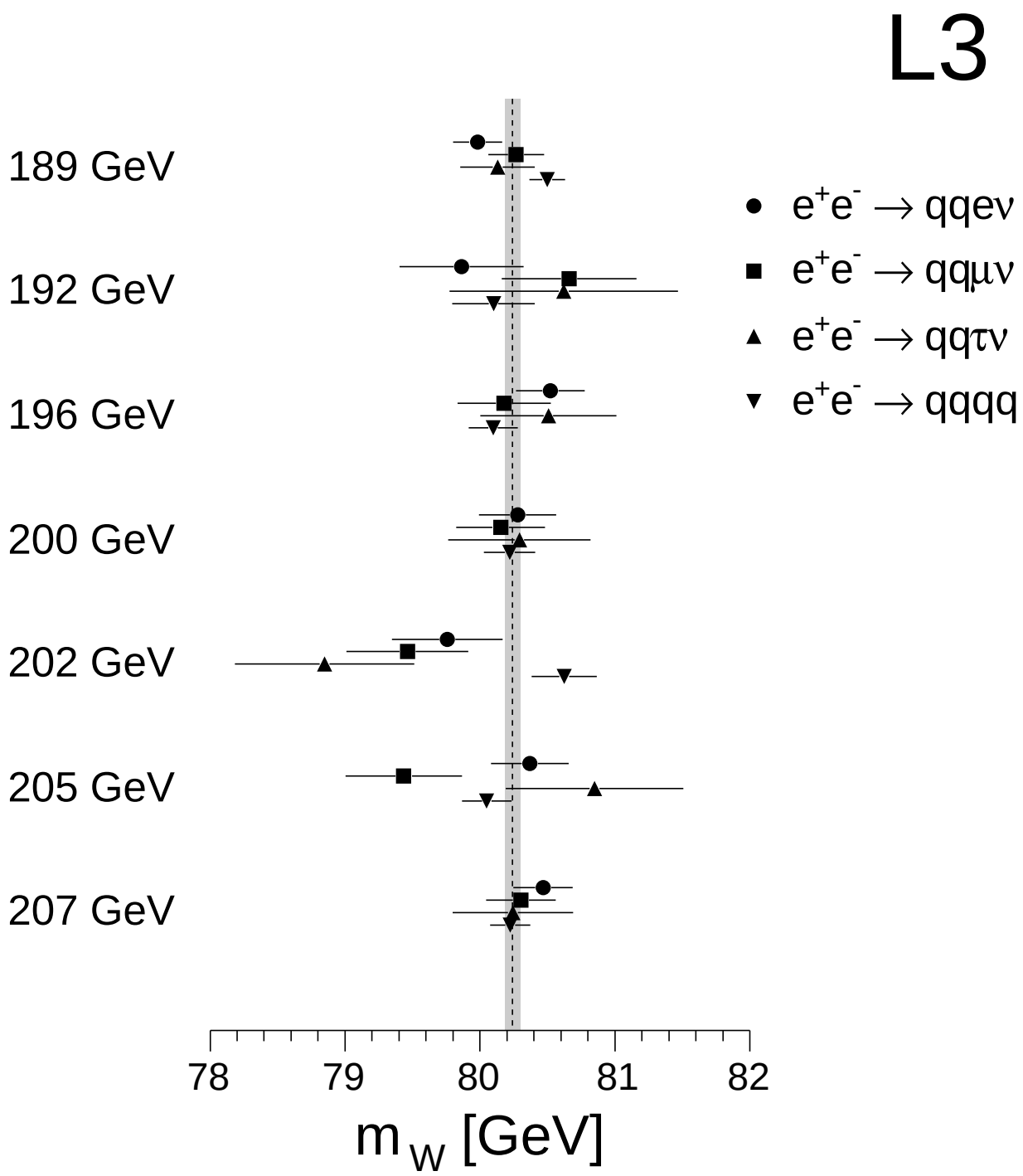

Figure 14: The results for m_{W} for the four final states and the seven average $\sqrt{s}$ values. Statistical and systematic uncertainties are added in quadrature. The combined m_{W} result and its uncertainty are indicated as the dashed line and the grey band, respectively.

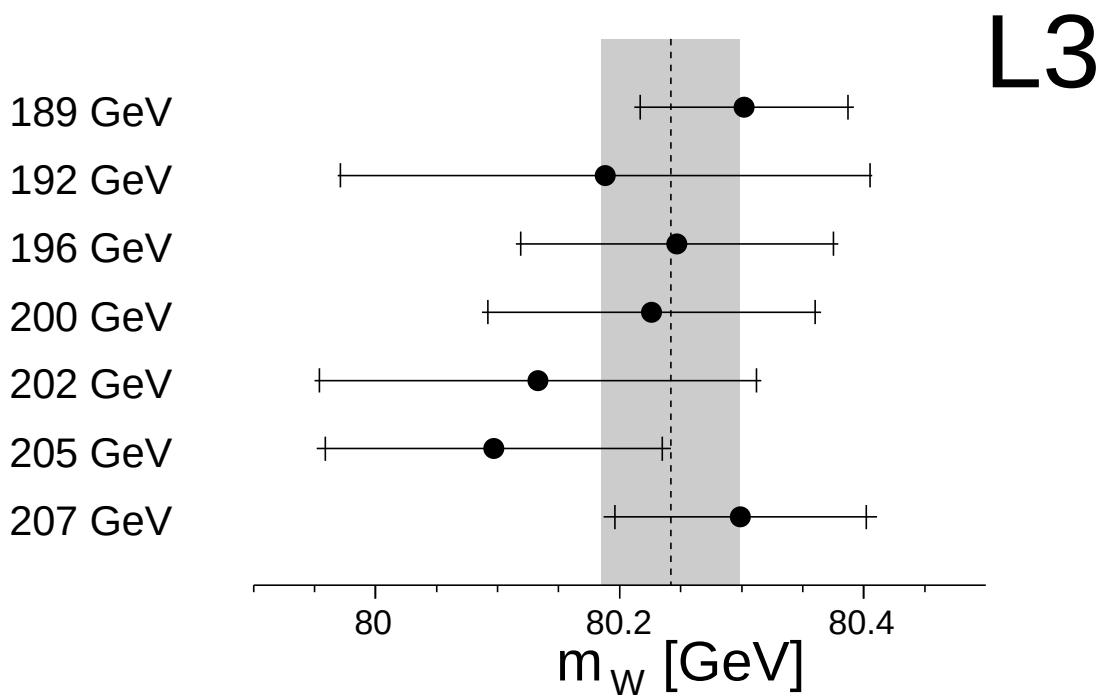

Figure 15: Comparison of the results for m_{W} for the seven average $\sqrt{s}$ values. The inner error bar represents the statistical uncertainty. The combined m_{W} result and its uncertainty are indicated as the dashed line and the grey band, respectively.

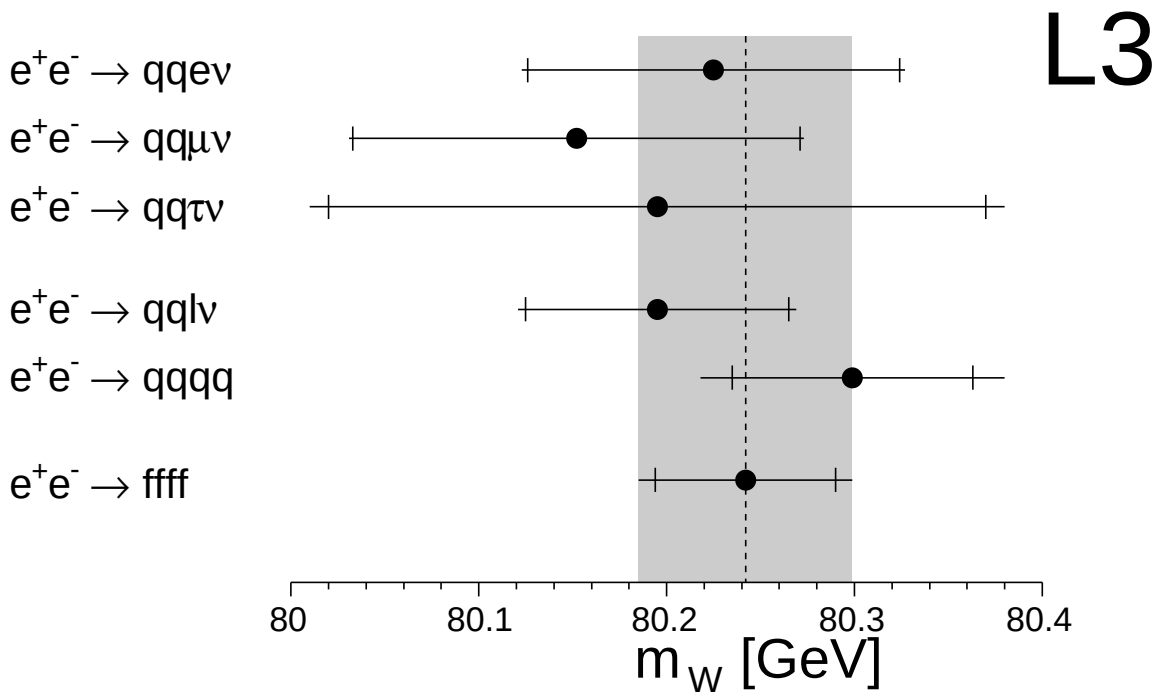

Figure 16: Comparison of the results for m_{W} for the $\sqrt{s} = 189-209$ GeV in each of the different final states. The inner error bar represents the statistical uncertainty.